The intrinsic alignment of galaxies: The good, the bad, and the ugly

Toshiki Kurita

March 20, 2025

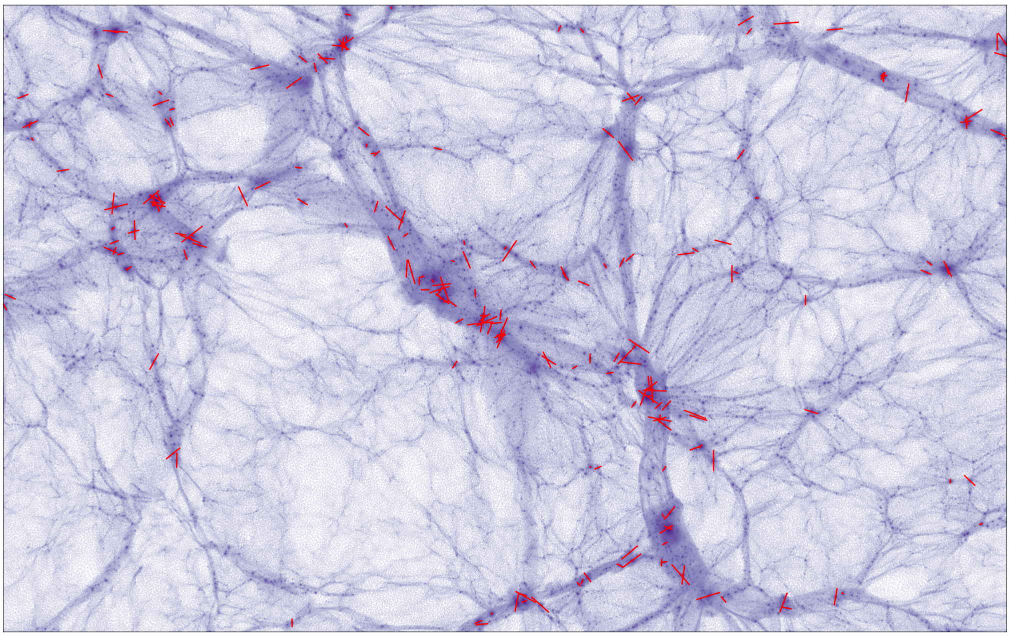

Figure 1: Snapshot of an 80×50 $(h^{-1}\mathrm{Mpc})^2$ slice with a thickness of 2 h^{-1}Mpc at redshift $z = 0.3$ from the IllustrisTNG300 simulation [1, 2]. The red rods represent simulated galaxies with stellar mass $M_* > 10^9$ $h^{-1}M_\odot$. The direction of each rod corresponds to the major axis of the projected galaxy ellipse, and the length is proportional to the magnitude of the ellipticity.

1 Introduction

In the standard ΛCDM scenario, the initial density fluctuations, which are the seeds of structure formation, are generated by inflation as adiabatic, Gaussian, and nearly scale-invariant perturbations. These fluctuations grow through gravitational instability, forming progressively larger structures as smaller ones merge repeatedly in a *bottom-up* process. This hierarchical growth eventually gives rise to the observed universe, including stars, galaxies, and galaxy clusters in the high-density regions formed through this process. The primary source of gravity in the structure formation is cold dark matter (CDM). As galaxies form under the influence of its gravitational (tidal) field, it has become evident that the intrinsic shapes of galaxies correlate with the surrounding large-scale structure. This physical correlation is known as *intrinsic alignments* (IA) [3, 4, 5, 6] (see Fig. 1).

Since IA can mimic part of the cosmic shear signal, they are considered a major systematic effect in cosmic shear analysis [7]. Many studies on IA have been motivated by its potential contamination of weak lensing measurements [see 8, 9, 10, 11, for a review]. Recently, however, IA has gained attention as a potential *cosmological signal* rather than just a contaminant. Several theoretical studies have explored the possibility of extracting cosmological information from IA effects. [e.g., 12, 13, 14]. While galaxy clustering analysis treats galaxies as "points" and focuses on their spatial distribution, IA provides additional cosmological information encoded in galaxy "shapes". If properly leveraged, IA could enhance constraints on cosmological parameters and offer a new probe into the physics of the early universe.

IA is fundamentally a physical correlation mediated by gravity on the *three-dimensional* shapes of galaxies and halos in *three-dimensional* space. Therefore, unlike weak lensing, which is essentially a *two-dimensional* phenomenon on the sky, IA naturally involves three-dimensional statistics, such as power spectra $P(k)$ or correlation functions $\xi(r)$, similar to galaxy clustering. On the other hand, the shape is a tensor quantity, not scalar quantity like galaxy density. Additionally, due to the projection onto the sky, it becomes a spin-2 quantity on the sky, similar to weak lensing shear, making techniques such as E/B decomposition useful. For these reasons, IA statistics lie between galaxy clustering and weak lensing, closely related to both, and have a unique structure both physically and mathematically.

This note is structured as follows: In Section 2, we define the "shapes" of galaxies and halos, and deepen our understanding of shape distortions and observational effects such as "projection" through simple examples. In Section 3, we introduce the linear theory that describes the distribution of galaxy and halo shapes and derive the expression for the IA power spectrum. We also discuss how this can serve as a potential cosmological signal. Then, in Section 4, we briefly introduce several advanced and related topics. Finally, in Section 5, we present an example of how IA can uniquely be sensitive to a particular type of primordial non-Gaussianity (PNG), which is more difficult to constrain using galaxy clustering or weak lensing.

2 What is the "shape" of a galaxy or halo?

2.1 Definition

We approximate the three-dimensional shape of a galaxy or dark matter halo, denoted as "g", as a *triaxial ellipsoid*, which is estimated from its second moment

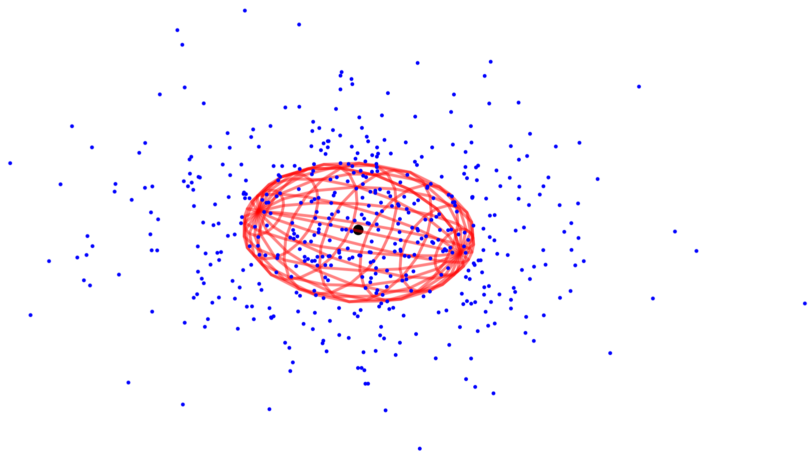

Figure 2: Particle distribution (blue points) and the ellipsoidal fit (red wireframe), obtained by measuring the second moment tensor (Eq. 1), with the contour level set to $C = 1$ as defined in Eq. (3). The black point represents the center of mass.

tensor (or inertia tensor):

$$I_{ij}(\mathbf{x}_{\rm g}) = \frac{1}{N} \int {\rm d}\mathbf{r} \rho_{\rm g}(\mathbf{r}) r_i r_j, \tag{1}$$

where $\rho_{\rm g}$ represents the mass density or luminosity profile of the object at the position $\mathbf{x}_{\rm g}$, and $\mathbf{r} \equiv \mathbf{x} - \mathbf{x}_{\rm g}$ is the position relative to its center. The normalization factor is somewhat arbitrary, but here it is defined as $N \equiv \int {\rm d}\mathbf{r} \rho_{\rm g}(\mathbf{r})$. In simulations, this tensor is estimated by summing over the member particles of the object. For the mass density ρ, it is given by:

$$I_{ij}(\mathbf{x}_{\rm g}) = \frac{1}{N} \sum_{\rm p \in g} m_{\rm p} (\mathbf{x}_{\rm p} - \mathbf{x}_{\rm g})_i (\mathbf{x}_{\rm p} - \mathbf{x}_{\rm g})_j, \tag{2}$$

where $m_{\rm p}$ and $\mathbf{x}_{\rm p}$ are the mass and position of a member particle p, and $N = \sum_{\rm p \in g} m_{\rm p}$ is the mass-weighted number of particles. Thus, I_{ij} corresponds to the *covariance* of the relative positions of the constituent elements. In this sense, the ellipsoidal fit of the particle distribution is given by

$$x_i I^{-1}_{ij} x_j = C, \tag{3}$$

where C determines the size of the contour. Fig. 2 shows an example of the ellipsoidal fit of a particle distribution. The off-diagonal components of I_{ij} represent the difference in orientation between the principal axes of deformation and the coordinate axes. By aligning the coordinate axes with the eigenvectors, the tensor can always be diagonalized, and thus we obtain the standard form of the ellipsoid in the new coordinates $\mathbf{x}'$:

$$\frac{x'^2_1}{\lambda_1} + \frac{x'^2_2}{\lambda_2} + \frac{x'^2_3}{\lambda_3} = C, \tag{4}$$

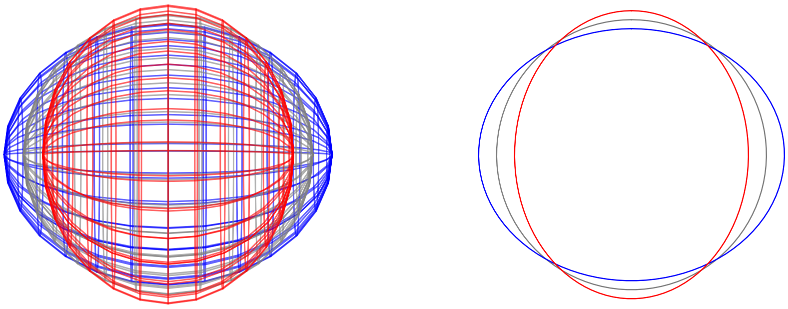

Figure 3: *Left panel*: Visualization of the distortion along the z-axis (horizontal in the figure) given by the trace-free part of Eq. (9). The blue and red ellipsoids correspond to $\Delta = +0.2$ and $\Delta = -0.2$, respectively, relative to the gray sphere. *Right panel*: A projection of the sphere and ellipsoid from the left panel onto a plane perpendicular to the line of sight (circle and ellipse).

where λ_i is the eigenvalue of I_{ij}.

I_{ij} is symmetric by definition (Eq. 1), meaning it has six degrees of freedom. Among these, one is the *trace* component, given by

$$\mathrm{Tr}I \equiv I_{11} + I_{22} + I_{33} = \lambda_1 + \lambda_2 + \lambda_3. \tag{5}$$

From Eq. (2), the trace can be expressed as

$$\mathrm{Tr}I = \frac{1}{N} \sum_{\mathrm{p}\in\mathrm{g}} m_\mathrm{p} \left|\mathbf{x}_\mathrm{p} - \mathbf{x}_\mathrm{g}\right|^2, \tag{6}$$

which represents the (weighted) mean squared distance of the relative positions. Since this serves as a measure of the dispersion from the center, it is generally considered to represent the "size" of the object. The remaining five degrees of freedom correspond to the *trace-free* component, defined as

$$I_{\langle ij\rangle} \equiv I_{ij} - \frac{\delta_{ij}}{3}\mathrm{Tr}I. \tag{7}$$

These components correspond to two modes of "deformation" that preserve volume (or size) and three parameters that determine the "orientation" of the principal axes (e.g., Euler angles).

Let us consider a spherically symmetric object where $I_{11} = I_{22} = I_{33} = \mathrm{Tr}I/3$ for simplicity, and examine the change in the diagonal component along the z-axis:

$$I_{33} \to I_{33}(1 + \Delta). \tag{8}$$

In this case, the trace and trace-free components change as follows:

$$
\begin{aligned}
I_{ij} + \Delta I_{ij} &= \frac{\mathrm{Tr} I}{3} \begin{pmatrix} 1 & 0 & 0 \\ 0 & 1 & 0 \\ 0 & 0 & 1+\Delta \end{pmatrix}_{ij} \\
&= \frac{\mathrm{Tr} I}{3} \begin{pmatrix} 1+\frac{\Delta}{3} & 0 & 0 \\ 0 & 1+\frac{\Delta}{3} & 0 \\ 0 & 0 & 1+\frac{\Delta}{3} \end{pmatrix}_{ij} + \frac{\mathrm{Tr} I}{3} \begin{pmatrix} -\frac{\Delta}{3} & 0 & 0 \\ 0 & -\frac{\Delta}{3} & 0 \\ 0 & 0 & +\frac{2\Delta}{3} \end{pmatrix}_{ij}
\end{aligned} \tag{9}
$$

Thus, the transformation in Eq. (8) scales the size (trace) by a factor of $1+\Delta/3$ and introduces the distortion proportional to Δ described in the second term above[1]. We show an example of this trace-free distortion in Fig. 3. When $\Delta > 0$, the distortion stretches along the z-axis, and when $\Delta < 0$, the distortion compresses along the z-axis. Note that the distortion around the z-axis is isotropic.

Such a decomposition into trace and trace-free components is an *irreducible decomposition*, which separates the degrees of freedom of a symmetric tensor based on their transformation properties under rotations (see below). Since intrinsic alignments describe the correlations in shape distortions and orientations of galaxies and halos, we will particularly focus on the trace-free component in the modeling presented in Section 3.

2.2 Projection

So far, we have considered the galaxy shape tensor I_{ij} defined in three-dimensional space. However, in actual observations, we observe only the "projected" shape of individual galaxies onto the sky, which lies on a two-dimensional plane perpendicular to the line-of-sight direction, under the flat-sky approximation, which is a good approximation since the size of a galaxy is very small compared to the curvature scale of the celestial sphere. See Fig. 4 for an illustration.

For simplicity, we first assume the line-of-sight direction to be $\hat{\mathbf{n}} = \hat{\mathbf{z}}$. In this case, the projection operator takes the form:

$$
\mathcal{P}_{ij}(\hat{\mathbf{z}}) = \delta_{ij} - \hat{z}_i \hat{z}_j = \begin{pmatrix} 1 & 0 & 0 \\ 0 & 1 & 0 \\ 0 & 0 & 0 \end{pmatrix}_{ij} . \tag{11}
$$

Note that $\mathcal{P}_{ij}$ acts as the identity tensor in this subspace, i.e., the two-dimensional plane normal to the line-of-sight direction, rather than δ_{ij} for the three-dimensional

[1]This distortion is often referred to as *quadrupolar* modulation since the trace-free part of the second moment tensor contributes to the quadrupolar component of the gravitational potential at large distances from the object (system), which is given by

$$
\phi^{(\ell=2)}(\mathbf{r}) \propto \frac{I_{\langle ij \rangle} \hat{r}_i \hat{r}_j}{r^3} = \frac{\mathrm{Tr} I}{3} \frac{\mathcal{L}_2(\mu)}{r^3} 2\Delta, \tag{10}
$$

where $\mu = \hat{\mathbf{r}} \cdot \hat{\mathbf{z}}$ and $\mathcal{L}_2$ is the Legendre polynomial of order 2.

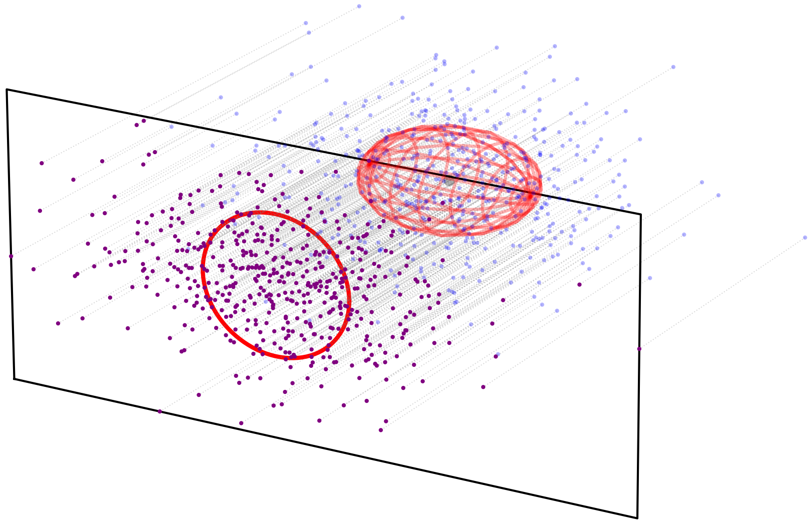

Figure 4: An example of the projection of a particle distribution onto a plane perpendicular to the line of sight. What we observe is the red ellipse on the screen, estimated from the projected particle distribution (purple points), while the depth information of the particle distribution is generally not an observable quantity.

space. Thus, the "projected" tensor is expressed as:

$$\gamma_{ij} \equiv \mathcal{P}_{ik}(\hat{\mathbf{z}})\mathcal{P}_{jl}(\hat{\mathbf{z}})I_{kl} = \begin{pmatrix} I_{11} & I_{12} & 0 \\ I_{21} & I_{22} & 0 \\ 0 & 0 & 0 \end{pmatrix}_{ij} . \tag{12}$$

where the orthogonality condition $\gamma_{ij}\hat{z}_j = 0$ holds. This constraint reduces the degrees of freedom from 6 to 3: one corresponds to the two-dimensional trace, $I_{11} + I_{22}$, while the remaining two are the trace-free components:

$$\gamma_1 \equiv \frac{I_{11} - I_{22}}{2}, \;\; \gamma_2 \equiv I_{12}. \tag{13}$$

These components can be mathematically extracted by:

$$\mathrm{Tr}\gamma = I_{11} + I_{22}, \tag{14}$$

$$\begin{aligned} \gamma_{\langle ij\rangle} &= \gamma_{ij} - \frac{\mathrm{Tr}\gamma}{2}\mathcal{P}_{ij}(\hat{\mathbf{z}}) \\ &= \begin{pmatrix} (I_{11} - I_{22})/2 & I_{12} & 0 \\ I_{21} & -(I_{11} - I_{22})/2 & 0 \\ 0 & 0 & 0 \end{pmatrix}_{ij} = \begin{pmatrix} \gamma_1 & \gamma_2 & 0 \\ \gamma_2 & -\gamma_1 & 0 \\ 0 & 0 & 0 \end{pmatrix}_{ij} . \end{aligned} \tag{15}$$

The two components γ_1 and γ_2 correspond to the distortions along the directions of coordinate axes (x or y) and the directions rotated by 45° from coordinate axes, respectively. See Fig. 5 for an illustration.

While the above expressions are specific to the case where the line-of-sight direction is $\hat{\mathbf{n}} = \hat{\mathbf{z}}$, the general projection for arbitrary $\hat{\mathbf{n}}$ can be obtained by replacing

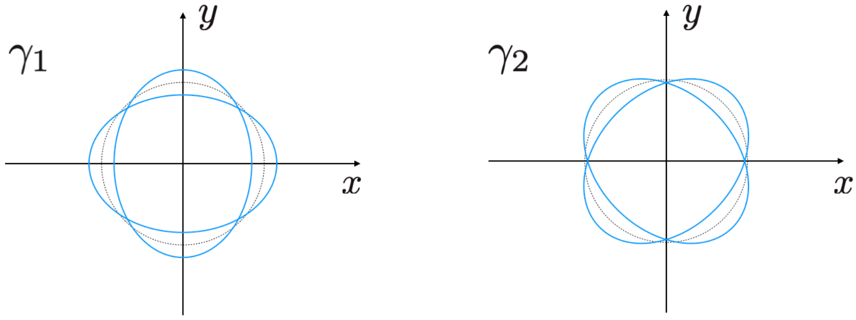

Figure 5: Illustration of the distortions induced by the two parameters, γ_1 (left) and γ_2 (right), after projection onto a two-dimensional plane. γ_1 corresponds to a distortion along the coordinate axes, where $\gamma_1 > 0$ indicates stretching in the x-direction and compression in the y-direction, while $\gamma_1 < 0$ corresponds to the opposite. Similarly, γ_2 represents a distortion oriented at a 45° angle to the axes, where positive values indicate stretching along one diagonal and compression along the other.

$\mathcal{P}_{ij}(\hat{\mathbf{z}}) \to \mathcal{P}_{ij}(\hat{\mathbf{n}})$. The mathematical operation to extract the trace-free component is then given by:

$$\gamma_{\langle ij\rangle}(\hat{\mathbf{n}}) = \gamma_{ij}(\hat{\mathbf{n}}) - \frac{\mathrm{Tr}\gamma(\hat{\mathbf{n}})}{2}\mathcal{P}_{ij}(\hat{\mathbf{n}}) \tag{16}$$

$$= \left(\mathcal{P}_{ik}(\hat{\mathbf{n}})\mathcal{P}_{jl}(\hat{\mathbf{n}}) - \frac{1}{2}\mathcal{P}_{ij}(\hat{\mathbf{n}})\mathcal{P}_{kl}(\hat{\mathbf{n}})\right) I_{kl} \tag{17}$$

$$\equiv \mathcal{P}_{ijkl}(\hat{\mathbf{n}}) I_{kl}. \tag{18}$$

Note that $\gamma_{\langle ij\rangle} = \mathcal{P}_{ijkl} I_{kl} = \mathcal{P}_{ijkl} I_{\langle kl\rangle}$. In this way, the "projection" is a purely observational effect, which can be considered as a mathematical operation applied to the three-dimensional shape I_{ij} after it is given, by applying the projector. Therefore, when modeling the underlying physical correlations of galaxy shapes, we first perform the modeling on the three-dimensional shape I_{ij}, and then consider this projection when dealing with actual observational quantities.

2.3 Fluctuation

Given a set of inertia tensors of a target sample $\{I_{ij,\mathrm{g}}\}_{\mathrm{g}=1,\cdots,N_\mathrm{g}}$, we formally define the inertia tensor *field* by assigning the values at each position as

$$I_{ij}(\mathbf{x}) \equiv \frac{1}{\bar{n}_\mathrm{g}} \sum_{\mathrm{g}} I_{ij,\mathrm{g}} \delta_\mathrm{D}(\mathbf{x} - \mathbf{x}_\mathrm{g}), \tag{19}$$

where $\bar{n}_{\rm g} \equiv N_{\rm g}/V$ is the mean number density of the sample[2].

To define the fluctuation, we first consider the one-point statistics of I_{ij}. Due to statistical isotropy, the shape of an object after the ensemble average must be spherically symmetric. This implies that the off-diagonal components vanish and that the eigenvalues must be equal in all directions, i.e.,

$$\langle I_{11}\rangle = \langle I_{22}\rangle = \langle I_{33}\rangle = \langle {\rm Tr}I\rangle/3, \tag{21}$$

and otherwise zero. Thus, the degrees of freedom reduce to a single parameter, the trace component (size), and we obtain

$$\langle I_{ij}\rangle = \frac{\langle {\rm Tr}I\rangle}{3}\delta_{ij}. \tag{22}$$

In practice, this ensemble average is estimated using the sample mean: $\langle {\rm Tr}I\rangle = 1/N_{\rm g}\sum_{\rm g}{\rm Tr}I_{\rm g}$.

Now, we define the dimensionless "fluctuation" of shape, S_{ij}, as the deviation from the ensemble average:

$$\delta_{ij} + S_{ij}(\mathbf{x}) \equiv \frac{I_{ij}(\mathbf{x})}{\langle {\rm Tr}I\rangle/3}. \tag{23}$$

This definition follows the same concept as defining the density fluctuation, $\delta_{\rm g}$, in galaxy clustering as

$$1 + \delta_{\rm g}(\mathbf{x}) \equiv \frac{n_{\rm g}(\mathbf{x})}{\langle n_{\rm g}\rangle}, \tag{24}$$

but with a key difference: while the density field is a *scalar* field, the shape field is a (rank-two) *tensor* field.

Now, for S_{ij}, we separate the trace part and the trace-free part as follows:

$$S_{ij}(\mathbf{x}) = \frac{{\rm Tr}S(\mathbf{x})}{3}\delta_{ij} + S_{\langle ij\rangle}(\mathbf{x}) \tag{25}$$

$$\equiv \delta_s(\mathbf{x})\delta_{ij} + S_{\langle ij\rangle}(\mathbf{x}). \tag{26}$$

We defined the size fluctuation as $\delta_s \equiv {\rm Tr}S/3$ in the second line. Here, we consider a rotation of the coordinate system: $x'_i = R_{ij}x_j$. Since δ_{ij} is an isotropic tensor ($\delta'_{ij} = R_{ii'}R_{jj'}\delta_{i'j'} = R_{ii'}R^{\rm T}_{i'j} = \delta_{ij}$), we have $\delta'_s(\mathbf{x}') = \delta_s(\mathbf{x})$, showing that the size

[2] A field constructed in this way, due to the properties of the Dirac delta function, satisfies

$$\hat{I}_{ij}(\mathbf{x}) = \frac{1}{\bar{n}_{\rm g}}\sum_{\rm g} I_{ij}(\mathbf{x}_{\rm g})\delta_{\rm D}(\mathbf{x}-\mathbf{x}_{\rm g}) = I_{ij}(\mathbf{x})\frac{1}{\bar{n}_{\rm g}}\sum_{\rm g}\delta_{\rm D}(\mathbf{x}-\mathbf{x}_{\rm g}) = I_{ij}(\mathbf{x})(1+\delta_{\rm g}(\mathbf{x})). \tag{20}$$

Thus, it can be interpreted as a field of the underlying $I_{ij}(\mathbf{x})$ sampled at the positions of galaxies $\{\mathbf{x}_{\rm g}\}_{{\rm g}=1,\cdots,N_{\rm g}}$. Therefore, strictly speaking, it represents a *density-weighted* field. However, in the linear theory that we will discuss, this effect is considered to be small and will be neglected going forward.

fluctuation is a "scalar" field. On the other hand, for the trace-free part, we have $S'_{\langle ij \rangle} = R_{ii'}R_{jj'}S_{\langle i'j' \rangle}$, This means that while the components mix, they do not mix with components outside of the trace-free part. As a result, the trace and trace-free parts can be separated in terms of their transformation properties under rotations. Since the theory model for the scalar field $\delta_s(\mathbf{x})$ has the same degrees of freedom as the galaxy density field $\delta_{\rm g}(\mathbf{x})$, it will be modeled using the same bias expansion as that for a scalar biased tracer of the large-scale structure (although the values of the bias coefficients may differ). In contrast, the trace-free part is inherently a tensorial tracer, so a bias expansion that accounts for its degrees of freedom, which is different from the scalar case, is required.

The Fourier transform of the shape field is defined as

$$S_{ij}(\mathbf{k}) \equiv \int \mathrm{d}\mathbf{x} S_{ij}(\mathbf{x}) e^{-i\mathbf{k}\cdot\mathbf{x}}, \tag{27}$$

$$S_{ij}(\mathbf{x}) \equiv \int \frac{\mathrm{d}\mathbf{k}}{(2\pi)^3} S_{ij}(\mathbf{k}) e^{i\mathbf{k}\cdot\mathbf{x}}, \tag{28}$$

The purpose here is to explore the cosmological information encoded in the statistics of the shape field.

3 Linear theory

3.1 Linear Alignment (LA) model

In this section, we introduce a physical model for $S_{ij}(\mathbf{x})$. As described in the definition of the Fourier transform (Eq. 28), $S_{ij}(\mathbf{x})$ can be expressed as a superposition of numerous Fourier modes. Among them, we are particularly interested in the contribution from cosmological, large-scale modes, such as those with a wavelength greater than $\lambda \sim 100h^{-1}$Mpc, corresponding to a wavenumber of $k = 2\pi/\lambda \sim 0.1\ h\mathrm{Mpc}^{-1}$. In other words, we hereafter implicitly assume a *low-pass filtered* shape field:

$$S^l_{ij}(\mathbf{x}) = \int \frac{\mathrm{d}\mathbf{k}}{(2\pi)^3} W_l(k) S_{ij}(\mathbf{k}) e^{i\mathbf{k}\cdot\mathbf{x}}, \tag{29}$$

where $W_l(k)$ is a low-pass filter that satisfies $W_l(k) = 1$ for sufficiently large scales (small k), and vanishes for smaller scales (large k).

For the galaxy at position $\mathbf{x}$, what could be the origin of the large-scale modes contributing to its shape, $S_{ij}(\mathbf{x})$? Since it is difficult for astrophysical processes to generate modes on scales much larger than those of galaxy and halo formation, any nonzero component on such large scales is expected to originate from primordial perturbations generated by inflation. As constrained by observations of the CMB and galaxy clustering, if the early universe contained only a single degrees of freedom (adiabatic scalar mode), then at large scales where linear theory holds, all fluctuations should be proportional to the single scalar field, e.g., the primordial gravitational potential $\Phi_{\rm p}(\mathbf{x})$[3]. Furthermore, for the large-scale modes we are

[3]We here also assume the Gaussian initial condition.

interested in, the region of galaxy and halo formation (or its Lagrangian patch) is considered to be sufficiently local. Therefore, the gravitational effects on galaxy formation, i.e., the observable gravitational effects on galaxies, are, at the lowest order, always related to the second derivative of the potential, $\partial_i\partial_j\Phi(\mathbf{x})$, along its trajectory.

From these considerations, in the linear regime, we assume the following linear relation to hold:

$$S_{ij}(\mathbf{x}) \propto \partial_i\partial_j\Phi(\mathbf{x}). \tag{30}$$

From here, we focus only on the trace-free component $S_{\langle ij\rangle}$, which we will simply denote as S_{ij}. The linear theory of intrinsic alignments is called the *linear alignment (LA) model*, which assumes that the three-dimensional tensor S_{ij} is linearly related to the second derivative of the potential [7]:

$$S_{ij}(\mathbf{x}) = b_K K_{ij}(\mathbf{x}), \tag{31}$$

where K_{ij} is the rescaled, dimensionless tidal field, defined as

$$K_{ij}(\mathbf{x}) \equiv \left(\partial_i\partial_j - \frac{\delta_{ij}}{3}\nabla^2\right)\frac{\Phi(\mathbf{x})}{4\pi G a^2\bar{\rho}_m(a)} \tag{32}$$

$$= \left(\frac{\partial_i\partial_j}{\nabla^2} - \frac{\delta_{ij}}{3}\right)\delta(\mathbf{x}), \tag{33}$$

or, equivalently, in Fourier space:

$$K_{ij}(\mathbf{k}) = \left(\hat{k}_i\hat{k}_j - \frac{\delta_{ij}}{3}\right)\delta(\mathbf{k}). \tag{34}$$

Here, a is the scale factor ($a = 1/(1+z)$), and $\bar{\rho}_{\mathrm{m}}(a)$ is the mean matter density at a. In the second equality, we have related the gravitational potential Φ to the matter density fluctuation δ via the Poisson equation:

$$\nabla^2\Phi(\mathbf{x}) = 4\pi G a^2\bar{\rho}_m(a)\delta(\mathbf{x}). \tag{35}$$

The coefficient b_K is called the *linear shape bias parameter*, which depends on the properties of the sample galaxies or halos, such as luminosity (for galaxies), mass, redshift, cosmological parameters, etc. The physical meaning of this linear bias can be interpreted as the *response* of the shape to the large-scale tidal field. Notably, Eq. (31) represents the tensor counterpart of the well-known linear bias relation in galaxy clustering:

$$\delta_{\mathrm{g}}(\mathbf{x}) = b_1\delta(\mathbf{x}). \tag{36}$$

Here, we aim to develop a clearer physical understanding of the LA model (Eq. 31). Without loss of generality, we consider a Fourier mode aligned with the

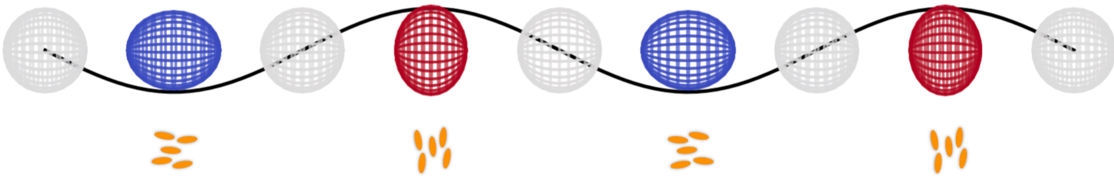

Figure 6: The distortion pattern of galaxy shapes predicted by the LA model. The black curve represents the large-scale Fourier modes along the z-axis (horizontal in the figure) extracted from the matter density field $\delta(\mathbf{x})$. The ellipsoids (blue and red) and the sphere (gray) represent the predicted distortion patterns created by this mode according to the LA model with $b_K < 0$. This is a statistical prediction, meaning that while individual galaxies (shown in orange) have scattered shapes, the large-scale pattern is statistically aligned.

z-axis, $\mathbf{k} = k\hat{\mathbf{z}}$. Based on the definition of the Fourier transform, the contribution of this mode to $S_{ij}(\mathbf{x})$ can be written as

$$S_{ij}(\mathbf{x}) \supset b_K \left(\hat{k}_i \hat{k}_j - \frac{\delta_{ij}}{3} \right) \delta(\mathbf{k}) e^{i\mathbf{k}\cdot\mathbf{x}} \bigg|_{\mathbf{k}=k\hat{\mathbf{z}}} = \begin{pmatrix} -\frac{1}{3} & 0 & 0 \\ 0 & -\frac{1}{3} & 0 \\ 0 & 0 & +\frac{2}{3} \end{pmatrix}_{ij} b_K \delta(\mathbf{k}) e^{ikz}. \tag{37}$$

This distortion takes the same form as Eq. (9), with an amplitude given by $\Delta = b_K \delta(\mathbf{k}) e^{ikz}$. Thus, the LA model predicts that a Fourier mode $\mathbf{k}$ induces a distortion *pattern* in the form of a plane wave with amplitude $b_K \delta(\mathbf{k})$ (see Fig. 6). Since this distortion is purely along the direction of $\hat{\mathbf{k}}$ and remains isotropic in the plane perpendicular to $\hat{\mathbf{k}}$, it is referred to as a *longitudinal scalar mode*.

Note that measurements of intrinsic alignment signals, obtained from both simulated galaxies/halos and observed galaxy shapes, indicate that $b_K < 0$. The negative sign implies that galaxy and halo shapes tend to be stretched along the minor axis of the tidal field. In other words, the principal major axis of the inertia tensor tends to align with filamentary structures or lie within sheet-like structures. This is consistent with an intuitive picture in which mass accretion occurs along the minor axis of the tidal field, naturally leading to an elongated shape in that direction.

3.2 Projection and E/B decomposition

So far, we have examined the three-dimensional distortion patterns. However, actual observables correspond to the projected two-dimensional shapes on the plane perpendicular to the line of sight (i.e., on the sky). As discussed in Section 2.2, this observational effect can be expressed as the contraction of the original three-dimensional shape tensor S_{ij} with the projection tensor given in Eq. (18). Here, we adopt the assumption that all galaxies share the same line-of-sight direction (the global-plane parallel limit or distant observer approximation) and take this direction to be along the z-axis. The two trace-free components of the projected shape tensor

γ_{ij} can then be obtained by applying the projection tensor to the definition of the linear alignment model (Eq. 31), yielding

$$\gamma_1(\mathbf{x}) = \frac{b_K}{2}\frac{\partial_1^2 - \partial_2^2}{\nabla^2}\delta(\mathbf{x}), \tag{38}$$

$$\gamma_2(\mathbf{x}) = b_K\frac{\partial_1\partial_2}{\nabla^2}\delta(\mathbf{x}), \tag{39}$$

Equivalently, we obtain the LA model in Fourier space,

$$\gamma_1(\mathbf{k}) = \frac{b_K}{2}\left(\hat{k}_1^2 - \hat{k}_2^2\right)\delta(\mathbf{k}) \tag{40}$$

$$= \frac{b_K}{2}(1-\mu^2)\cos 2\phi_{\mathbf{k}}\delta(\mathbf{k}), \tag{41}$$

$$\gamma_2(\mathbf{k}) = b_K\hat{k}_1\hat{k}_2\delta(\mathbf{k}) \tag{42}$$

$$= \frac{b_K}{2}(1-\mu^2)\sin 2\phi_{\mathbf{k}}\delta(\mathbf{k}), \tag{43}$$

where $\mu \equiv \hat{\mathbf{k}}\cdot\hat{\mathbf{z}} = \hat{k}_3$ and $\phi_{\mathbf{k}} \equiv \tan^{-1}(\hat{k}_1/\hat{k}_2)$ is the phase factor rotating the tensor components on the plane perpendicular to the line-of-sight direction in Fourier space.

An important point to note is that the coordinates of the field, $\mathbf{x}$ and $\mathbf{k}$, are *three-dimensional*, and the "projection" acts only on the components of the tensor (i.e., its internal degrees of freedom), not on the position. Conceptually, this corresponds to considering the *three-dimensional* spatial distribution of *two-dimensionally* projected ellipses, as illustrated in Fig. 7. In observations, such a shape field is realized by combining spectroscopic and imaging surveys. For galaxies with spectroscopic redshifts (and thus three-dimensional positions) obtained from the spectroscopic survey, the imaging data (two ellipticities) are assigned to the corresponding positions of each galaxy, allowing for the construction of $\gamma_1(\mathbf{x})$ and $\gamma_2(\mathbf{x})$. This is a key distinction from weak lensing statistics (such as the angular power spectrum), where both the galaxy positions and shapes are projected onto a two-dimensional space.

For later convenience, we here introduce the complex representation of the shear components:

$$\begin{aligned} {}_{\pm 2}\gamma(\mathbf{k}) &\equiv \gamma_1(\mathbf{k}) \pm i\gamma_2(\mathbf{k}) \\ &= \frac{b_K}{2}(1-\mu^2)e^{\pm 2i\phi_{\mathbf{k}}}\delta(\mathbf{k}). \end{aligned} \tag{44}$$

Here, let us consider a rotation of the coordinate axes around the line-of-sight direction $\hat{\mathbf{z}}$ by an angle θ. $\delta(\mathbf{k})$ is a scalar, we have $\delta'(\mathbf{k}') = \delta(\mathbf{k})$, and $\mu' = \hat{\mathbf{k}}'\cdot\hat{\mathbf{z}} = \mu$ is also invariant under this rotation. On the other hand, since the phase changes as $\phi_{\mathbf{k}'} = \phi_{\mathbf{k}} - \theta$, ${}_{\pm 2}\gamma$ ($\gamma_{1,2}$) are *coordinate-dependent* quantities, specifically called as *spin-2* quantities on the sky due to their transformation property: ${}_{\pm 2}\gamma' = {}_{\pm 2}\gamma e^{\mp 2i\theta}$. To obtain a *coordinate-independent* quantity, we define the E-mode and B-mode fields by rotating ${}_{\pm 2}\gamma$ in Fourier space and canceling the phase factors as

$$E(\mathbf{k}) \pm iB(\mathbf{k}) \equiv {}_{\pm 2}\gamma(\mathbf{k})e^{\mp 2i\phi_{\mathbf{k}}}. \tag{45}$$

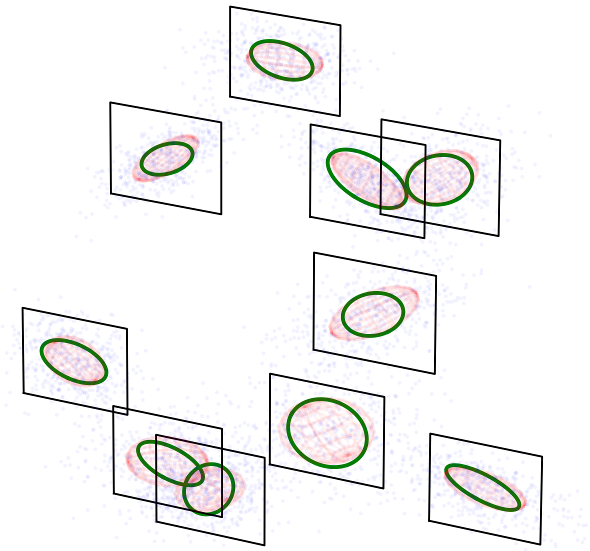

Figure 7: An example of the three-dimensional spatial distribution of two-dimensional shapes (green ellipses). Each ellipse corresponds to the projected shape of a galaxy as observed in imaging surveys, with the distribution of these shapes in three-dimensional space resulting from the combination of spectroscopic redshift (providing the galaxy's position) and imaging data (providing the ellipticities).

These fields are invariant under any rotations around the line-of-sight direction. In Fig. 8, we show the E/B-mode patterns in real space. The distortion direction represented by the E mode is either parallel or perpendicular to the wave vector (horizontal), while the distortion direction represented by the B mode is tilted by 45 degrees.

Substituting Eq. (44) into Eq. (45), we obtain the LA model for the E and B-mode fields:

$$E(\mathbf{k}) = \frac{b_K}{2}(1-\mu^2)\delta(\mathbf{k}), \tag{46}$$

$$B(\mathbf{k}) = 0. \tag{47}$$

Thus, the LA model generates only the E-mode as the galaxy shape pattern. This means that, in the linear regime, the E-mode is a physical mode caused by the scalar gravitational potential, while the B-mode is a non-physical mode that cannot be generated by the scalar mode, and therefore serves as an indicator of systematic errors in actual measurements. Note that the B-mode can be generated in the nonlinear regime, as shown in the intrinsic alignment power spectrum below.

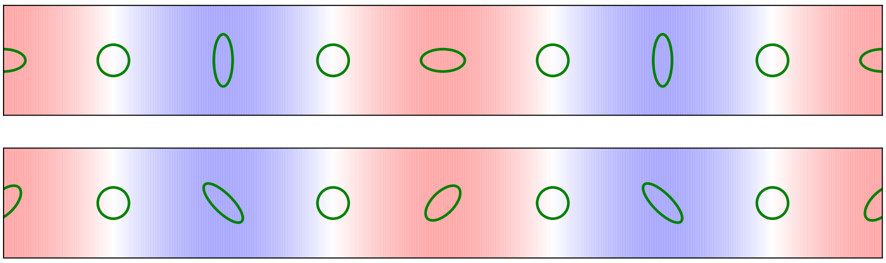

Figure 8: Green ellipses represent the E-mode (top) and B-mode (bottom) patterns in real space, i.e., $E(\mathbf{x})$ and $B(\mathbf{x})$, generated by a plane wave, with the Fourier mode direction oriented to the right. That is, the E-mode (B-mode) distortion corresponds to γ_1 (γ_2) distortion, rotated such that the Fourier mode direction aligns with the x-axis.

3.3 Power spectrum

Let's now define the intrinsic alignment power spectrum from the following three fields we currently have:

$$\{\delta_{\rm g}(\mathbf{k}), E(\mathbf{k}), B(\mathbf{k})\}\,. \tag{48}$$

Their auto- and cross-power spectra are defined as

$$\langle X(\mathbf{k})Y(\mathbf{k}')\rangle \equiv (2\pi)^3\delta_D(\mathbf{k}+\mathbf{k}')P_{XY}(\mathbf{k}), \tag{49}$$

where X, Y represent field labels. Here, we assume linear theory for both the density field and intrinsic alignment. (We first consider the real-space case and then take into account redshift space distortions.) For example, the density–E-mode cross-power spectrum and the E-mode auto-power spectrum are given by

$$P_{\rm gE}(k,\mu) = b_1\frac{b_K}{2}(1-\mu^2)P_{\rm lin}(k), \tag{50}$$

$$P_{\rm EE}(k,\mu) = \frac{b_K^2}{4}(1-\mu^2)^2P_{\rm lin}(k), \tag{51}$$

where $P_{\rm lin}$ is the linear matter power spectrum. All spectra involving the B-mode are zero in linear theory. Note that, once again, although the E/B modes are defined as distortion patterns on the two-dimensional plane perpendicular to the line-of-sight direction, the power spectra are given as a function of the three-dimensional wavevector, $\mathbf{k}$.

In addition, the power spectra depend not only on the scalar wavenumber k ($= |\mathbf{k}|$) but also on the direction of $\mathbf{k}$, particularly through the factor $(1-\mu^2)$, where $\mu = \hat{\mathbf{k}}\cdot\hat{\mathbf{z}}$ is the cosine of the angle between the Fourier mode direction and the line-of-sight direction. This factor arises from the projection of shapes

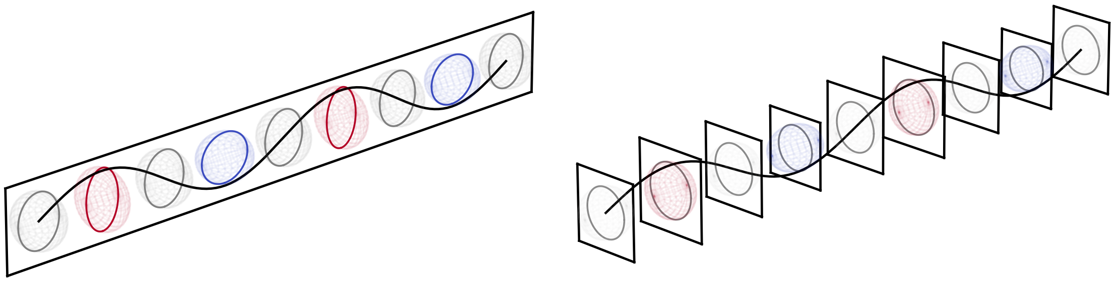

Figure 9: Projection of the three-dimensional galaxy shape distortion pattern predicted by the LA model along the line of sight. The left and right panels show the projected two-dimensional shape patterns for the same Fourier mode but with different line-of-sight directions: the left panel corresponds to a line of sight perpendicular to the Fourier mode ($\mu = 0$), while the right panel corresponds to a line of sight parallel to the Fourier mode ($\mu = 1$).

(Eqs. 41 and 43) and represents an observational effect. A visual explanation of the anisotropy introduced by this projection is shown in Fig. 9. For example, the distortion pattern created by a Fourier mode $\mathbf{k}$ perpendicular to the line of sight ($\mu = 0$, left panel) remains observable after projection (since $1-\mu^2 = 1 \neq 0$). On the other hand, the pattern generated by a Fourier mode $\mathbf{k}$ parallel to the line of sight ($\mu = 1$, right panel) becomes completely isotropic after projection and thus cannot be observed (since $1 - \mu^2 = 0$)[4]. Therefore, the intrinsic alignment power spectra are already anisotropic in real space, even before considering the effects of redshift-space distortion, due to the projection effect. These power spectra contain the full information on the intrinsic alignment effect at the level of two-point statistics.

For convenience in actual measurements and analyses, we define the multipole moments of the power spectra as

$$P^{(\ell)}_{XY}(k) \equiv (2\ell + 1) \int_{-1}^{1} \frac{\mathrm{d}\mu}{2} \mathcal{L}_\ell(\mu) P_{XY}(k, \mu), \tag{52}$$

where $\mathcal{L}_\ell$ is the Legendre polynomials of order ℓ. From Eqs. (50) and (51), we obtain for the cross spectrum:

$$P^{(0)}_{\mathrm{gE}}(k) = \frac{1}{3} b_1 b_K P_{\mathrm{lin}}(k), \tag{53}$$

$$P^{(2)}_{\mathrm{gE}}(k) = -P^{(0)}_{\mathrm{gE}}(k), \tag{54}$$

[4]However, the size fluctuation of the projected two-dimensional shape remains, in principle, observable. Here, we focus on the distortion (the trace-free part) and thus ignore this effect.

and for the auto spectrum:

$$P_{\mathrm{EE}}^{(0)}(k) = \frac{2}{15} b_K^2 P_{\mathrm{lin}}(k), \tag{55}$$

$$P_{\mathrm{EE}}^{(2)}(k) = -\frac{10}{7} P_{\mathrm{EE}}^{(0)}(k), \tag{56}$$

$$P_{\mathrm{EE}}^{(4)}(k) = \frac{3}{7} P_{\mathrm{EE}}^{(0)}(k). \tag{57}$$

These anisotropic intrinsic alignment power spectra have actually been measured from simulations [see e.g., 15, for measurements in N-body simulations].

Next, let us consider the redshift-space distortion. Due to peculiar velocities, the position of galaxies in the line-of-sight direction is inferred to deviate from the isotropic Hubble flow. However, the observed galaxy shape itself remains invariant (at leading order) since it involves components perpendicular to the line-of-sight direction. In other words, in the linear regime, the galaxy density field is only affected by the Kaiser effect. Therefore, the linear power spectrum in redshift space only modifies the cross-power spectrum, and we obtain:

$$P_{\mathrm{gE}}^{(\mathrm{S})}(k,\mu) = (b_1 + f\mu^2)\frac{b_K}{2}(1-\mu^2)P_{\mathrm{lin}}(k), \tag{58}$$

where

$$\delta_{\mathrm{g}}^{(\mathrm{S})}(\mathbf{k}) = (b_1 + f\mu^2)\delta(\mathbf{k}), \tag{59}$$

with $f \equiv \mathrm{dln}D/\mathrm{dln}a$ being the linear growth rate and D being the linear growth factor. An interesting observation can be made by comparing Eqs. (46) and (59). Both are anisotropic with respect to the line-of-sight direction, but while intrinsic alignment is sensitive to the component perpendicular to the line-of-sight ($\mu = 0$), galaxy density is sensitive to the component parallel to the line-of-sight ($\mu = 1$). This difference in anisotropy suggests that using both the galaxy clustering and intrinsic alignment signals could lead to tighter constraints, such as on $f\sigma_8$ [16]. Furthermore, as seen from the expression in linear theory, the intrinsic alignment power spectrum, like galaxy clustering, depends on P_{lin}, meaning it is also sensitive to baryon acoustic oscillations (BAO) [17]. Therefore, stronger constraints on the geometrical parameters, the Hubble parameter $H(z)$ and angular-diameter distance $d_A(z)$, are also expected through the distortion of the BAO via the Alcock–Paczynski effect [14].

4 Additional Topics

4.1 Beyond the LA model

Here we summarize some IA models beyond the linear alignment model.

- *Nonlinear alignment model (NLA)*: Ref. [18] proposed an empirical model based on the linear alignment model where the linear matter power spectrum appearing in Eqs. (50) and (51) is replaced with the nonlinear matter power spectrum, $P_{\rm lin}(k) \to P_{\rm NL}(k)$, where $P_{\rm NL}$ is provided by `halofit` [19] for instance. This model has been found to fit the measured IA correlation function well down to $r \sim 2\ h^{-1}$Mpc [e.g., 20] and commonly adopted to model the IA contamination in the recent cosmic shear analyses [e.g., 21].

- *Perturbation theory-based models*: In order to predict the IA effect beyond the linear theory, one might want to use the perturbation theory of structure formation [22] and the bias expansion for cosmological tracers [23]. For example, Ref. [24] proposed the "Tidal Alignment + Tidal Torquing" (TATT) model which includes the quadratic terms:

$$\begin{aligned} S_{ij}(\mathbf{x}) &= b_K K_{ij}(\mathbf{x}) \\ &\quad + b_{\delta K}\delta(\mathbf{x})K_{ij}(\mathbf{x}) + b_{KK}\left(K_{ik}(\mathbf{x})K_{kj}(\mathbf{x}) - \frac{1}{3}\delta^K_{ij}K^2(\mathbf{x})\right) + b_T T_{ij}(\mathbf{x}). \end{aligned} \tag{60}$$

  where the first term corresponds to the linear alignment model, the second is for the density-weighted tidal field, the third is for the tidal torque effect, and the fourth is defined as $T_{ij} \equiv (\partial_i\partial_j/\nabla^2 - \delta^K_{ij}/3)(\delta^2 - K^2)$, which form a complete basis at second order [see 25, 26, for further discussion]. This model recently has been used in the cosmic shear analyses as well as the NLA model [e.g., 27, 28]. More recently, Ref. [29] developed an effective field theory (EFT) description including the higher order derivatives and stochastic contributions from the small-scale modes up to one-loop order [see also 30, 31].

- *Halo model*: To model the IA signal of galaxies in the inner region of their host dark matter halos, i.e. the one-halo term, Ref. [32] provided the fitting function with a halo model-based approach by using N-body simulations under the two assumptions that the shapes of the central galaxies trace those of dark matter halos at the central part and the shapes of the satellite galaxies point at their halo center. The fitting formula is characterized by three parameters, except the overall amplitude $a^{1h}_{\rm IA}$, as

$$P^{1h}_{\rm mE}(k) = a^{1h}_{\rm IA}\frac{(k/p_1)^2}{1 + (k/p_2)^{p_3}}, \tag{61}$$

  where $p_i = q_{i_1}\exp\left(q_{i_2} z^{q_{i_3}}\right)$ and z is the redshift. These parameters are shown in Table 2 in Ref. [32]. Ref. [20] showed that the measured correlation function can be explained by the hybrid model of the NLA model and this halo model down to $r_\perp \sim 0.1\ h^{-1}$Mpc. Recently, Ref. [33] improved the halo model including the luminosity and color dependence of galaxies.

4.2 Direct measurements

We briefly introduce some pioneering studies on the direct measurements of IA.

4.2.1 Observational Constraints: Early-Type Galaxies

Early-type galaxies are groups of old stars, hence often red galaxies, that have completed star formation. The luminous red galaxies (LRGs) have been the main target of BAO searches of spectroscopic galaxy surveys [e.g. SDSS, 34] because they can be easily identified to high redshifts. The three-dimensional shape of early-type galaxies, especially elliptical galaxies, is generally considered to be a triaxial ellipsoid. Since it is difficult to support such a shape with rotational motion, the shape of elliptical galaxies is actually supported by the anisotropic random motion (velocity dispersion) of stars. Therefore, shape correlations are considered to be described by the "tidal stretching" picture in the linear alignment model due to the lack of angular momentum.

The direct measurements of the IA correlations from LRGs have been done in Ref. [35] and many works [e.g., 36, 37, 38, 39, 20] investigated the IA correlations using SDSS LRG samples. In particular, Ref. [20] carried out a comprehensive study using the SDSS BOSS LOWZ sample, and found that the hybrid model with the NLA model and the halo model successfully explains the measured IA correlation function over $0.1 < r_\perp < 100\ h^{-1}$Mpc. They also investigated the dependence of the IA amplitude (b_K or $A_{\rm IA}$) on the properties and environments of galaxy samples, e.g. luminosity, color, redshift, central/satellite, and gave a fitting function of the luminosity of galaxies [see also 38].

4.2.2 Misalignment between galaxy and halo shapes

Here we mention the connection of shapes of galaxies and their host dark matter halos following Ref. [37]. By using the halo catalogs constructed from N-body simulations, Ref. [37] generated the SDSS LRG-like galaxy mock catalogs using the halo occupation distribution (HOD) method [40, 41, 42, 43]. The central galaxies in their mock catalogs inherit the shape information from their host dark matter halos assuming an imperfect inheritance of orientation, the so-called *misalignment*, between galaxy and halo that is characterized by a Gaussian random distribution as

$$f(\theta;\sigma_\theta)\mathrm{d}\theta = \frac{1}{\sqrt{2\pi}\sigma_\theta}\exp\left[-\frac{1}{2}\left(\frac{\theta}{\sigma_\theta}\right)^2\right], \tag{62}$$

where θ is the misalignment angle between the major axes and σ_θ is a parameter describing a typical misalignment angle for a galaxy sample. By measuring the IA correlation function from this LRG-like mock sample and comparing it with the actual measurements, they obtained $\sigma_\theta = 35^\circ \pm 2^\circ$ which leads to a degradation of the alignment signal by a factor of two. Interestingly, although this "random-scatter" misalignment model can only change an overall constant factor to the correlation function, the mock signal also reproduces the scale dependence of the actual data quite well. Thus, this result gives observational evidence that galaxy shapes are very closely related to the shapes of their host halos in a sense of large-scale correlations.

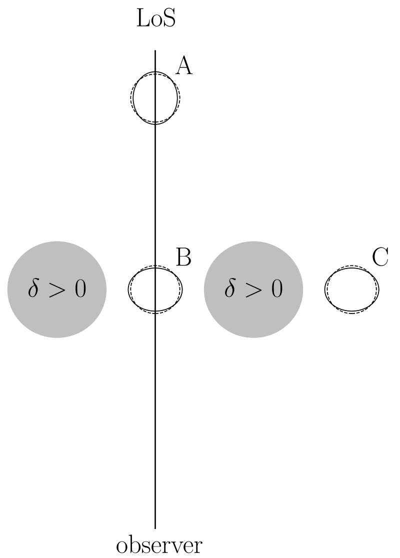

Figure 10: A schematic illustration of weak lensing and intrinsic alignment effects. Ellipses (A, B, C) represent observed galaxy shapes. A distant galaxy (A) is distorted by weak lensing from the mass distribution along the light cone (gray region). Galaxies (B, C) at lower redshift are deformed by the same mass distribution via the IA effect. The GI and II terms correspond to correlations between A and B (or C), and between B and C, respectively.

The misalignment angle has been recently investigated in hydrodynamic simulations [e.g. 44, 45] and shown to be $\sigma_\theta \sim 30^\circ$ for both red and blue galaxies.

4.2.3 Observational Constraints: Late-Type Galaxies

Late-type galaxies consist of a central ellipsoidal component called a bulge and a broadened disk component. The observed shape is determined by the projection of the disk onto the celestial sphere and thus depends on its inclination and the line-of-sight directions. The disk is supported by angular momentum which requires at least second-order effects, the so-called tidal torque in Eq. (60) since the linear theory can not produce a rotational motion. Hence the large-scale correlations in late-type galaxies are expected to be smaller than those in early-type galaxies. Actually the correlation functions have been measured for late-type galaxies in observations, but have not yet been detected [e.g. 36, 46]. These results are consistent with recent hydrodynamic simulations [e.g. 47].

4.3 Systematic effects on weak lensing analysis

Correlations between observed galaxy images distorted by weak gravitational lensing effects, called cosmic shear, are a unique method of revealing the inhomogeneous dark matter distribution in the universe. Since the IA correlation of galaxies mimics part of this correlation [7], if we assume that the observed shape correlations are purely due to lensing effects, the constraints on cosmological parameters could be biased. Most of the previous studies on IA have been motivated by these possible systematic effects on the weak lensing analysis. We here briefly show how the IA affects the weak lensing analysis.

Including the weak gravitational lensing (G) and intrinsic alignment (I) effects, the observed galaxy shape can be written by

$$\gamma^{\rm obs} = \gamma^{\rm G} + \gamma^{\rm I}, \tag{63}$$

where we assumed that both of the distortions are sufficiently small [48]. The angular power spectrum of the observed galaxy shapes then includes three terms as

$$C_\ell^{\rm obs} = C_\ell^{\rm GG} + C_\ell^{\rm II} + C_\ell^{\rm GI}, \tag{64}$$

where GG is the pure weak lensing signal due to the foreground large-scale structure from source galaxies to us, II is the auto IA signal due to the local tidal field in the region where source galaxies live, i.e., surrounding large-scale structure, and GI is the cross-correlation which arises when the same large-scale structure can be responsible for both the lensing effect on galaxies with higher redshifts and the IA effect on those with lower redshifts due to a broad redshift distribution of photometric galaxy samples. In Fig. 10, we show a schematic picture of this contamination effect. Note that with a point mass lens (or shperical mass distribution), the weak lensing effect predicts tangential shear around the mass, while the IA effect predicts radial shear. Hence the GI correlation should be negative.

5 Primordial non-Gaussianity in galaxy shapes

5.1 Local-type primordial non-Gaussianity

In the standard ΛCDM scenario, the primordial fluctuation field, such as the Bardeen potential Φ [49], which sets the initial conditions for structure formation, is predicted to follow a Gaussian distribution under the standard inflationary scenario. The statistical properties of such a Gaussian field are fully characterized by its power spectrum (or equivalently, the two-point correlation function):

$$\langle \Phi(\mathbf{k}_1)\Phi(\mathbf{k}_2)\rangle = (2\pi)^3\delta_{\rm D}(\mathbf{k}_1+\mathbf{k}_2)P_\phi(k_1). \tag{65}$$

Here, the primordial potential Φ is related to the curvature perturbation ζ as $\Phi = 3\zeta/5$. In linear theory, the matter density fluctuation $\delta(\mathbf{k}, z)$ is related to the primordial fluctuation via

$$\delta(\mathbf{k}, z) = \mathcal{M}(k, z)\Phi(\mathbf{k}), \tag{66}$$

where

$$\mathcal{M}(k, z) \equiv \frac{2}{3}\frac{k^2\mathcal{T}(k)D(z)}{\Omega_{\rm m}H_0^2}, \tag{67}$$

with $\mathcal{T}(k)$ being the transfer function and $D(z)$ the linear growth factor, normalized to the scale factor in the matter-dominated era. For simplicity, we omit the redshift dependence of δ and $\mathcal{M}$ hereafter. Since $\mathcal{T}(k) \to 1$ for $k \ll k_{\rm eq}$, where $k_{\rm eq} \sim 0.015\ h{\rm Mpc}^{-1}$ [50] corresponds to the horizon scale at matter-radiation equality, $\mathcal{M}(k)$ scales as $\propto k^2$ at large scales.

Primordial non-Gaussianity (PNG) is defined as any deviation from Gaussianity, with the leading-order effect characterized by the bispectrum:

$$\langle \Phi(\mathbf{k}_1)\Phi(\mathbf{k}_2)\Phi(\mathbf{k}_3)\rangle = (2\pi)^3\delta_{\rm D}(\mathbf{k}_1+\mathbf{k}_2+\mathbf{k}_3)B_\Phi(\mathbf{k}_1,\mathbf{k}_2,\mathbf{k}_3). \tag{68}$$

We assume that the non-Gaussian fluctuation Φ can be expressed as a local function of a Gaussian random field ϕ:

$$\Phi(\mathbf{x}) = \mathcal{F}[\phi(\mathbf{x})]. \tag{69}$$

Given that $|\phi| \ll 1$, the leading non-Gaussian contribution, based on a Taylor expansion, is given by

$$\Phi(\mathbf{x}) = \phi(\mathbf{x}) + f_{\rm NL}\left(\phi^2(\mathbf{x}) - \langle\phi^2\rangle\right), \tag{70}$$

where the subtraction of $\langle\phi^2\rangle$ ensures $\langle\Phi\rangle = 0$. Substituting Eq. (70) into Eq. (68), we obtain

$$B_\Phi(\mathbf{k}_1,\mathbf{k}_2,\mathbf{k}_3) = 2f_{\rm NL}P_\phi(k_1)P_\phi(k_2) + 2\ \text{perms}. \tag{71}$$

This simplest quadratic non-Gaussianity is known as the "local-type" PNG [51], and the amplitude parameter $f_{\rm NL}$ has been constrained by CMB bispectrum measurements [e.g., 52, 53, 54, 55, 56].

5.2 Scale-dependent bias in galaxy clustering

Using Eq. (67), we obtain the matter bispectrum at leading order:

$$B_{\rm m}(\mathbf{k}_1,\mathbf{k}_2,\mathbf{k}_3) = \mathcal{M}(k_1)\mathcal{M}(k_2)\mathcal{M}(k_3)B_\phi(\mathbf{k}_1,\mathbf{k}_2,\mathbf{k}_3). \tag{72}$$

An important property of Eq. (72) is that it has a large amplitude in the so-called *squeezed* triangle configuration, where one of the three modes, e.g., $\mathbf{k}_3$, is much larger than the other two, i.e., $\mathbf{k}_1 \simeq \mathbf{k}_2 \gg \mathbf{k}_3$. In this limit, Eq. (72) simplifies to

$$B_{\rm m}(\mathbf{k}_1,\mathbf{k}_2,\mathbf{k}_3) = 4f_{\rm NL}\mathcal{M}^{-1}(k)P(k)P(q) + \mathcal{O}\left(\frac{k}{q}\right)^2, \tag{73}$$

where P is the matter power spectrum, and we have relabeled the long mode as $\mathbf{k} \equiv \mathbf{k}_3$ and the short modes as $\mathbf{k}_1, \mathbf{k}_2 \equiv \mathbf{q} \pm \mathbf{k}/2$. This squeezed bispectrum can be equivalently interpreted as the modulation of the local (or short-mode) matter power spectrum at position $\mathbf{x}$ in the presence of a long-mode realization due to mode coupling:

$$P(q;\mathbf{x}) = \left[1 + 4f_{\rm NL}\phi_\ell(\mathbf{x})\right]P(q). \tag{74}$$

We can reproduce Eq. (73) by correlating Eq. (74) with $\delta(\mathbf{k})$ in Fourier space. In terms of the σ_8 parameter, the local σ_8 is given by

$$\sigma_8(\mathbf{x}) = [1 + 2f_{\rm NL}\phi_\ell(\mathbf{x})]\sigma_8. \tag{75}$$

Fig. 11 shows an illustration for this modulation. In the presence of the local PNG, the local abundance of dark matter halos, hence galaxies, $n(\mathbf{x})$ depends not only on the long-mode density fluctuation $\delta_\ell(\mathbf{x})$ but also on $\sigma_8(\mathbf{x})$ through mode coupling with $\phi_\ell(\mathbf{x})$ (Eq. 74). The local number density, $n(\mathbf{x}) = n[\delta_\ell(\mathbf{x}), \sigma_8(\mathbf{x})]$, can be perturbatively expanded as

$$n(\mathbf{x}) = \bar{n} + \frac{\partial n}{\partial \delta_\ell}\delta_\ell(\mathbf{x}) + \frac{\partial n}{\partial \sigma_8}\delta\sigma_8(\mathbf{x}) = \bar{n}\left(1 + \frac{\partial \ln n}{\partial \delta_\ell}\delta_\ell(\mathbf{x}) + 2f_{\rm NL}\frac{\partial \ln n}{\partial \ln \sigma_8}\phi_\ell(\mathbf{x})\right). \tag{76}$$

From this, we obtain the linear (Lagrangian) bias for local PNG:

$$b_1(k; f_{\rm NL}) = b_1 + b_\phi f_{\rm NL}\mathcal{M}^{-1}(k), \tag{77}$$

where we define the bias in the Gaussian case as $b_1 \equiv \partial \ln n/\partial \delta_\ell$ and the PNG-induced bias as $b_\phi \equiv 2\partial \ln n/\partial \ln \sigma_8$[5].

Since the scale dependence is determined by $\mathcal{M}^{-1}(k) \propto k^{-2}$ at large scales, we can place strong constraints on $f_{\rm NL}$ using the large-scale galaxy power spectrum.

5.3 Scale-dependent bias in galaxy shapes

We consider here a generalized local-type PNG characterized by the bispectrum [57, 13]:

$$B_\Phi(\mathbf{k}_1, \mathbf{k}_2, \mathbf{k}_3) = 2\sum_{s=0,1,2,\cdots} f_{\rm NL}^{(s)}\left[\mathcal{L}_s(\hat{\mathbf{k}}_1 \cdot \hat{\mathbf{k}}_2)P_\phi(k_1)P_\phi(k_2) + 2 \text{ perms}\right], \tag{79}$$

where $\mathcal{L}_s$ is the Legendre polynomials of order s. The coefficient $f_{\rm NL}^{(s)}$ characterizes the amplitude of the local PNG at each order s. The term corresponding to $s = 0$, referred to as the *isotropic* term, matches the conventional local PNG case (Eq. 71). To distinguish it from other terms, we henceforth denote the conventional parameter $f_{\rm NL}$ as $f_{\rm NL}^{(0)}$. Here, we focus on the *anisotropic* PNG described by the $s = 2$ term in the above bispectrum:[6]

$$B_\Phi(\mathbf{k}_1, \mathbf{k}_2, \mathbf{k}_3) = 2f_{\rm NL}^{(2)}\mathcal{L}_2(\hat{\mathbf{k}}_1 \cdot \hat{\mathbf{k}}_2)P_\phi(k_1)P_\phi(k_2) + 2 \text{ perms}. \tag{80}$$

---

[5] Although we have considered the halo abundance in the initial fluctuation, i.e. Lagrangian space, we actually obtain the observebles at late time, i.e. in Eulerian space. The number conservation of the matter and halo are given by

$$[1 + \delta(\mathbf{x}^{\rm E})]\mathrm{d}\mathbf{x}^{\rm E} = \mathrm{d}\mathbf{x}^{\rm L},\ [1 + \delta_{\rm h}^{\rm E}(\mathbf{x}^{\rm E})]\mathrm{d}\mathbf{x}^{\rm E} = [1 + \delta_{\rm h}^{\rm L}(\mathbf{x}^{\rm L})]\mathrm{d}\mathbf{x}^{\rm L}. \tag{78}$$

Using these, we finally obtain the Eulerian bias as $b_1^{\rm E} \equiv 1 + b_1^{\rm L}$ at leading order. Hereafter we omit $^{\rm E}$ and use b_1 to refer to the Eulerian bias for simplicity.

[6] The anisotropic PNG can be generated in several inflationary scenarios: the solid inflation [58], the non-Bunch-Davies initial states [59], and the existence of vector fields [60, 61, 62, 57, 63] and higher-spin fields [64, 65, 66] in the inflationary epoch. Although the predicted bispectrum generally has a particular scale dependence such as $\mathcal{L}_\ell(\hat{\mathbf{k}}_1 \cdot \hat{\mathbf{k}}_2) \to (k_1/k_2)^{\Delta_\ell}\mathcal{L}_\ell(\hat{\mathbf{k}}_1 \cdot \hat{\mathbf{k}}_2)$ in Eq. (79), we consider a model with $\Delta_2 = 0$ for simplicity.

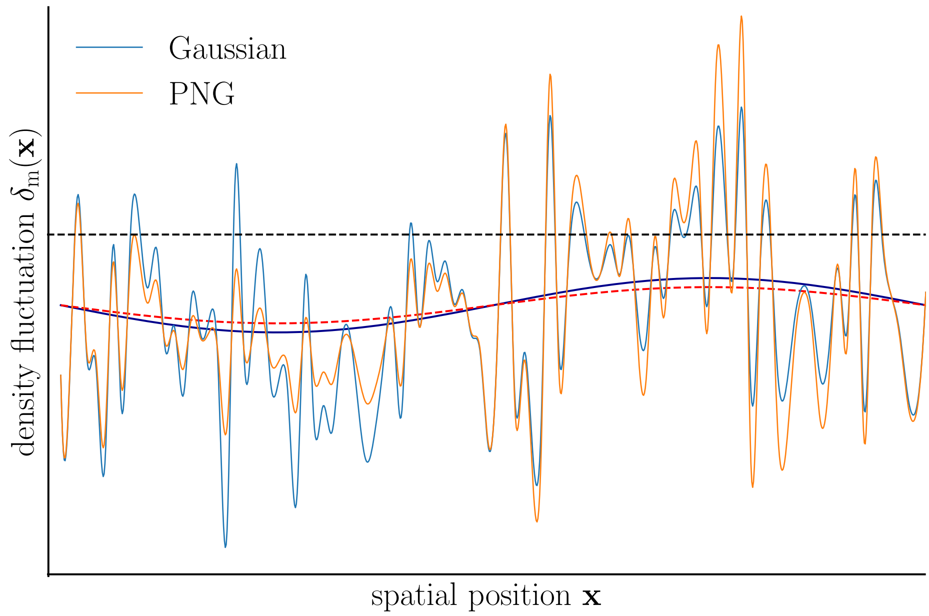

Figure 11: A schematic picture of the effect of PNG on the density fluctuation. The light-blue and orange lines correspond to short-mode fluctuations with and without local-type PNG, respectively. The dark-blue and red-dashed curves represent the large-scale mode of the density δ_ℓ and primordial potential ϕ_ℓ, respectively. The black-dashed line represents the threshold indicating high-density regions where dark matter halos, hence galaxies, form in the peak-background split picture. Since the short- and long- Fourier modes are independent in the Gaussian initial condition, the statistical amplitude of short-mode fluctuations, or power spectrum, does not depend on spatial position (light-blue). On the other hand, in the presence of the non-Gaussianity (orange), the amplitude of *local* short-mode spatially varies with respect to the underlying long-mode fluctuation ($\delta_\ell(\mathbf{x})$ or $\phi_\ell(\mathbf{x})$) due to the mode coupling (Eq. 74), which leads to the scale-dependent bias relation between the halo (galaxy) number density field and the density field.

In analogy with the isotropic case shown in Eqs. (72)-(74), the presence of anisotropic PNG modulates the amplitude of the local small-scale power spectrum at position $\mathbf{x}$, depending on the long-wavelength potential [13]:

$$P(\mathbf{q};\mathbf{x}) = \left[1 + 4f_{\rm NL}^{(2)}\psi_{ij,\ell}(\mathbf{x})\hat{q}_i\hat{q}_j\right] P(q), \tag{81}$$

where $\psi_{ij,\ell}$ is a trace-free tensor with the same dimension as ϕ_ℓ, defined as

$$\psi_{ij,\ell}(\mathbf{x}) \equiv \frac{3}{2}\left[\frac{\partial_i\partial_j}{\nabla^2} - \frac{1}{3}\delta^{\rm K}_{ij}\right]\phi_\ell(\mathbf{x}) = \frac{3}{2}\int_{\mathbf{k}}\left(\hat{k}_i\hat{k}_j - \frac{1}{3}\delta^{\rm K}_{ij}\right)\phi_\ell(\mathbf{k})e^{i\mathbf{k}\cdot\mathbf{x}}. \tag{82}$$

Since $\psi_{ij,\ell}$ is trace-free, it induces an anisotropic (quadrupolar) modulation in the power of short-mode fluctuations. In other words, the anisotropic PNG induces the coupling between the local tidal field, $K_{ij}(\mathbf{x})$, and the long-wavelength quadrupolar potential, $\psi_{ij}(\mathbf{x})$.

Recalling the definition of the linear shape bias in Gaussian initial conditions (Eq. 31):

$$S_{ij}(\mathbf{x}) = b_K K_{ij}(\mathbf{x}), \tag{83}$$

or, equivalently, by using the definition of S_{ij} (Eq. 23):

$$\frac{I_{ij}(\mathbf{x})}{\langle {\rm Tr}I\rangle/3} = \delta_{ij} + b_K K_{ij}(\mathbf{x}), \tag{84}$$

the parameter b_K can be interpreted as the response of shapes of local peaks, where galaxies and halos form, to large-scale modulation: $b_K \equiv \partial I_{kl}/\partial K_{kl}$. In the case of the anisotropic PNG, since the local peak shapes depend on both $K_{ij}(\mathbf{x})$ and $\psi_{ij}(\mathbf{x})$, i.e., $I_{ij}(\mathbf{x}) = I_{ij}[K_{ij}(\mathbf{x}), \psi_{ij}(\mathbf{x})]$ we obtain the scale-dependent shape bias in the linear regime:

$$b_K(k; f_{\rm NL}^{(2)}) = b_K + b_\psi f_{\rm NL}^{(2)}\mathcal{M}^{-1}(k), \tag{85}$$

where we denote the response of shapes to the anisotropic PNG as b_ψ.

In Ref. [67], N-body simulations with the PNGs confirm that the anisotropic ($s = 2$) PNG induces a scale-dependent modification in the IA power spectra in the low-k regime compared to Gaussian simulations (see Fig. 12). However, it does not affect the halo (clustering) power spectrum at the same scales. On the other hand, the isotropic ($s = 0$) PNG does not alter the IA power spectra but does modify the halo spectrum [68]. Thus, the scale-dependent bias in the IA power spectra is a unique signature arising from the anisotropy of PNG. If detected, it would serve as smoking-gun evidence for $s = 2$ PNG. In Ref. [69], the IA power spectrum was measured using the SDSS BOSS galaxy sample, and constraints on anisotropic PNG were obtained based on the signal in the linear regime.

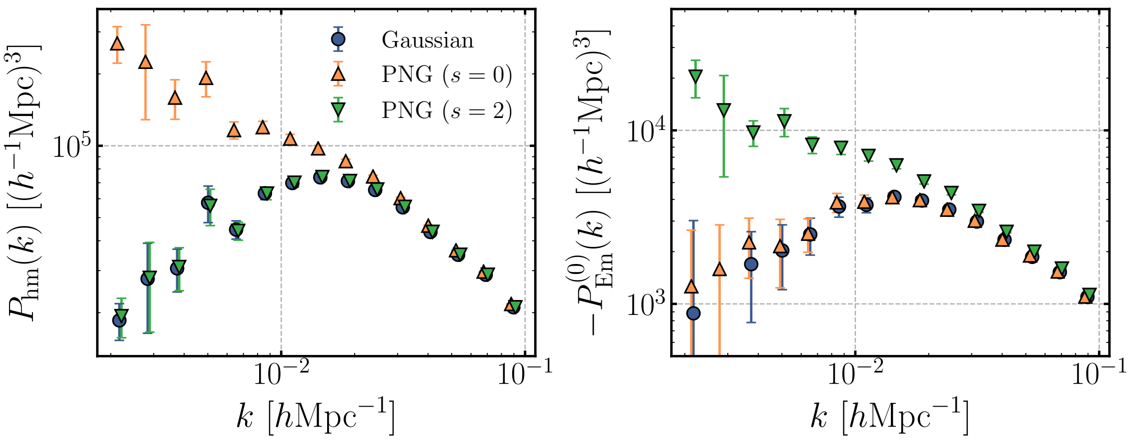

Figure 12: The matter-halo power spectrum (left panel) and the monopole moment of the matter-halo shape cross-power spectrum (E-mode) (right panel) for different initial conditions: Gaussian (blue), isotropic PNG (orange), and anisotropic PNG (green). For the isotropic and anisotropic PNG cases, we assume $(f_{\rm NL}^{s=0}, f_{\rm NL}^{s=2}) = (500, 0)$ and $(0, 500)$, respectively, following Eq. 79. These measurements are based on a halo sample with $M_{\rm vir} > 10^{14} h^{-1} M_\odot$ at $z = 0$. Adapted from Figure 1 in Ref. [67], with modifications.

References

[1] Volker Springel, Rüdiger Pakmor, Annalisa Pillepich, Rainer Weinberger, Dylan Nelson, Lars Hernquist, Mark Vogelsberger, Shy Genel, Paul Torrey, Federico Marinacci, and Jill Naiman. First results from the IllustrisTNG simulations: matter and galaxy clustering. MNRAS, 475(1):676–698, March 2018.

[2] Dylan Nelson, Volker Springel, Annalisa Pillepich, Vicente Rodriguez-Gomez, Paul Torrey, Shy Genel, Mark Vogelsberger, Ruediger Pakmor, Federico Marinacci, Rainer Weinberger, Luke Kelley, Mark Lovell, Benedikt Diemer, and Lars Hernquist. The IllustrisTNG simulations: public data release. *Computational Astrophysics and Cosmology*, 6(1):2, May 2019.

[3] Rupert A. C. Croft and Christopher A. Metzler. Weak-Lensing Surveys and the Intrinsic Correlation of Galaxy Ellipticities. ApJ, 545(2):561–571, Dec 2000.

[4] Paolo Catelan, Marc Kamionkowski, and Roger D. Blandford. Intrinsic and extrinsic galaxy alignment. MNRAS, 320(1):L7–L13, Jan 2001.

[5] Robert G. Crittenden, Priyamvada Natarajan, Ue-Li Pen, and Tom Theuns. Discriminating Weak Lensing from Intrinsic Spin Correlations Using the Curl-Gradient Decomposition. ApJ, 568(1):20–27, Mar 2002.

[6] Y. P. Jing and Yasushi Suto. Triaxial Modeling of Halo Density Profiles with High-Resolution N-Body Simulations. ApJ, 574(2):538–553, Aug 2002.

[7] Christopher M. Hirata and Uroš Seljak. Intrinsic alignment-lensing interference as a contaminant of cosmic shear. Phys. Rev. D, 70(6):063526, Sep 2004.

[8] Benjamin Joachimi, Marcello Cacciato, Thomas D. Kitching, Adrienne Leonard, Rachel Mandelbaum, Björn Malte Schäfer, Cristóbal Sifón, Henk Hoekstra, Alina Kiessling, Donnacha Kirk, and Anais Rassat. Galaxy Alignments: An Overview. Space Sci. Rev., 193(1-4):1–65, Nov 2015.

[9] Alina Kiessling, Marcello Cacciato, Benjamin Joachimi, Donnacha Kirk, Thomas D. Kitching, Adrienne Leonard, Rachel Mandelbaum, Björn Malte Schäfer, Cristóbal Sifón, Michael L. Brown, and Anais Rassat. Galaxy Alignments: Theory, Modelling & Simulations. Space Sci. Rev., 193(1-4):67–136, Nov 2015.

[10] Donnacha Kirk, Michael L. Brown, Henk Hoekstra, Benjamin Joachimi, Thomas D. Kitching, Rachel Mand elbaum, Cristóbal Sifón, Marcello Cacciato, Ami Choi, Alina Kiessling, Adrienne Leonard, Anais Rassat, and Björn Malte Schäfer. Galaxy Alignments: Observations and Impact on Cosmology. Space Sci. Rev., 193(1-4):139–211, Nov 2015.

[11] M. A. Troxel and Mustapha Ishak. The intrinsic alignment of galaxies and its impact on weak gravitational lensing in an era of precision cosmology. Phys. Rep., 558:1–59, Feb 2015.

[12] Fabian Schmidt and Donghui Jeong. Large-scale structure with gravitational waves. II. Shear. Phys. Rev. D, 86(8):083513, October 2012.

[13] Fabian Schmidt, Nora Elisa Chisari, and Cora Dvorkin. Imprint of inflation on galaxy shape correlations. *Journal of Cosmology and Astro-Particle Physics*, 2015(10):032, Oct 2015.

[14] Atsushi Taruya and Teppei Okumura. Improving geometric and dynamical constraints on cosmology with intrinsic alignments of galaxies. *The Astrophysical Journal*, 891(2):L42, Mar 2020.

[15] Toshiki Kurita, Masahiro Takada, Takahiro Nishimichi, Ryuichi Takahashi, Ken Osato, and Yosuke Kobayashi. Power spectrum of halo intrinsic alignments in simulations. *Monthly Notices of the Royal Astronomical Society*, 501(1):833–852, Nov 2020.

[16] Teppei Okumura and Atsushi Taruya. First Constraints on Growth Rate from Redshift-Space Ellipticity Correlations of SDSS Galaxies at $0.16 < z < 0.70$. *arXiv e-prints*, page arXiv:2301.06273, January 2023.

[17] Kun Xu, Y. P. Jing, Gong-Bo Zhao, and Antonio J. Cuesta. Evidence for baryon acoustic oscillations from galaxy-ellipticity correlations. *Nature Astronomy*, 7:1259–1264, October 2023.

[18] Sarah Bridle and Lindsay King. Dark energy constraints from cosmic shear power spectra: impact of intrinsic alignments on photometric redshift requirements. *New Journal of Physics*, 9(12):444, Dec 2007.

[19] Ryuichi Takahashi, Masanori Sato, Takahiro Nishimichi, Atsushi Taruya, and Masamune Oguri. Revising the Halofit Model for the Nonlinear Matter Power Spectrum. ApJ, 761(2):152, December 2012.

[20] Sukhdeep Singh, Rachel Mandelbaum, and Surhud More. Intrinsic alignments of SDSS-III BOSS LOWZ sample galaxies. MNRAS, 450(2):2195–2216, Jun 2015.

[21] Chiaki Hikage, Masamune Oguri, Takashi Hamana, Surhud More, Rachel Mandelbaum, Masahiro Takada, Fabian Köhlinger, Hironao Miyatake, Atsushi J. Nishizawa, Hiroaki Aihara, Robert Armstrong, James Bosch, Jean Coupon, Anne Ducout, Paul Ho, Bau-Ching Hsieh, Yutaka Komiyama, François Lanusse, Alexie Leauthaud, Robert H. Lupton, Elinor Medezinski, Sogo Mineo, Shoken Miyama, Satoshi Miyazaki, Ryoma Murata, Hitoshi Murayama, Masato Shirasaki, Cristóbal Sifón, Melanie Simet, Joshua Speagle, David N. Spergel, Michael A. Strauss, Naoshi Sugiyama, Masayuki Tanaka, Yousuke Utsumi, Shiang-Yu Wang, and Yoshihiko Yamada. Cosmology from cosmic shear power spectra with Subaru Hyper Suprime-Cam first-year data. PASJ, 71(2):43, April 2019.

[22] F. Bernardeau, S. Colombi, E. Gaztañaga, and R. Scoccimarro. Large-scale structure of the Universe and cosmological perturbation theory. Phys. Rep., 367(1-3):1–248, September 2002.

[23] Vincent Desjacques, Donghui Jeong, and Fabian Schmidt. Large-scale galaxy bias. Phys. Rep., 733:1–193, February 2018.

[24] Jonathan A. Blazek, Niall MacCrann, M. A. Troxel, and Xiao Fang. Beyond linear galaxy alignments. Phys. Rev. D, 100(10):103506, November 2019.

[25] Jonathan Blazek, Zvonimir Vlah, and Uroš Seljak. Tidal alignment of galaxies. *Journal of Cosmology and Astro-Particle Physics*, 2015(8):015, Aug 2015.

[26] D. M. Schmitz, C. M. Hirata, J. Blazek, and E. Krause. Time evolution of intrinsic alignments of galaxies. *Journal of Cosmology and Astro-Particle Physics*, 2018(7):030, Jul 2018.

[27] M. A. Troxel, N. MacCrann, J. Zuntz, T. F. Eifler, E. Krause, S. Dodelson, D. Gruen, J. Blazek, O. Friedrich, S. Samuroff, J. Prat, L. F. Secco, C. Davis, A. Ferté, J. DeRose, A. Alarcon, A. Amara, E. Baxter, M. R. Becker, G. M. Bernstein, S. L. Bridle, R. Cawthon, C. Chang, A. Choi, J. De Vicente, A. Drlica-Wagner, J. Elvin-Poole, J. Frieman, M. Gatti, W. G. Hartley, K. Honscheid, B. Hoyle, E. M. Huff, D. Huterer, B. Jain, M. Jarvis, T. Kacprzak,

D. Kirk, N. Kokron, C. Krawiec, O. Lahav, A. R. Liddle, J. Peacock, M. M. Rau, A. Refregier, R. P. Rollins, E. Rozo, E. S. Rykoff, C. Sánchez, I. Sevilla-Noarbe, E. Sheldon, A. Stebbins, T. N. Varga, P. Vielzeuf, M. Wang, R. H. Wechsler, B. Yanny, T. M. C. Abbott, F. B. Abdalla, S. Allam, J. Annis, K. Bechtol, A. Benoit-Lévy, E. Bertin, D. Brooks, E. Buckley-Geer, D. L. Burke, A. Carnero Rosell, M. Carrasco Kind, J. Carretero, F. J. Castander, M. Crocce, C. E. Cunha, C. B. D'Andrea, L. N. da Costa, D. L. DePoy, S. Desai, H. T. Diehl, J. P. Dietrich, P. Doel, E. Fernandez, B. Flaugher, P. Fosalba, J. García-Bellido, E. Gaztanaga, D. W. Gerdes, T. Giannantonio, D. A. Goldstein, R. A. Gruendl, J. Gschwend, G. Gutierrez, D. J. James, T. Jeltema, M. W. G. Johnson, M. D. Johnson, S. Kent, K. Kuehn, S. Kuhlmann, N. Kuropatkin, T. S. Li, M. Lima, H. Lin, M. A. G. Maia, M. March, J. L. Marshall, P. Martini, P. Melchior, F. Menanteau, R. Miquel, J. J. Mohr, E. Neilsen, R. C. Nichol, B. Nord, D. Petravick, A. A. Plazas, A. K. Romer, A. Roodman, M. Sako, E. Sanchez, V. Scarpine, R. Schindler, M. Schubnell, M. Smith, R. C. Smith, M. Soares-Santos, F. Sobreira, E. Suchyta, M. E. C. Swanson, G. Tarle, D. Thomas, D. L. Tucker, V. Vikram, A. R. Walker, J. Weller, Y. Zhang, and DES Collaboration. Dark Energy Survey Year 1 results: Cosmological constraints from cosmic shear. Phys. Rev. D, 98(4):043528, August 2018.

[28] S. Samuroff, J. Blazek, M. A. Troxel, N. MacCrann, E. Krause, C. D. Leonard, J. Prat, D. Gruen, S. Dodelson, T. F. Eifler, M. Gatti, W. G. Hartley, B. Hoyle, P. Larsen, J. Zuntz, T. M. C. Abbott, S. Allam, J. Annis, G. M. Bernstein, E. Bertin, S. L. Bridle, D. Brooks, A. Carnero Rosell, M. Carrasco Kind, J. Carretero, F. J. Castander, C. E. Cunha, L. N. da Costa, C. Davis, J. De Vicente, D. L. DePoy, S. Desai, H. T. Diehl, J. P. Dietrich, P. Doel, B. Flaugher, P. Fosalba, J. Frieman, J. García-Bellido, E. Gaztanaga, D. W. Gerdes, R. A. Gruendl, J. Gschwend, G. Gutierrez, D. L. Hollowood, K. Honscheid, D. J. James, K. Kuehn, N. Kuropatkin, M. Lima, M. A. G. Maia, M. March, J. L. Marshall, P. Martini, P. Melchior, F. Menanteau, C. J. Miller, R. Miquel, R. L. C. Ogando, A. A. Plazas, E. Sanchez, V. Scarpine, R. Schindler, M. Schubnell, S. Serrano, I. Sevilla-Noarbe, E. Sheldon, M. Smith, F. Sobreira, E. Suchyta, G. Tarle, D. Thomas, V. Vikram, and DES Collaboration. Dark Energy Survey Year 1 results: constraints on intrinsic alignments and their colour dependence from galaxy clustering and weak lensing. MNRAS, 489(4):5453–5482, November 2019.

[29] Zvonimir Vlah, Nora Elisa Chisari, and Fabian Schmidt. An EFT description of galaxy intrinsic alignments. J. Cosmology Astropart. Phys., 2020(1):025, January 2020.

[30] Zvonimir Vlah, Nora Elisa Chisari, and Fabian Schmidt. Galaxy shape statistics in the effective field theory. *Journal of Cosmology and Astroparticle Physics*, 2021(05):061, May 2021.

[31] Shi-Fan Chen and Nickolas Kokron. A Lagrangian theory for galaxy shape statistics. J. Cosmology Astropart. Phys., 2024(1):027, January 2024.

[32] Michael D. Schneider and Sarah Bridle. A halo model for intrinsic alignments of galaxy ellipticities. MNRAS, 402(4):2127–2139, Mar 2010.

[33] Maria Cristina Fortuna, Henk Hoekstra, Benjamin Joachimi, Harry Johnston, Nora Elisa Chisari, Christos Georgiou, and Constance Mahony. The halo model as a versatile tool to predict intrinsic alignments. MNRAS, 501(2):2983–3002, February 2021.

[34] Donald G. York, J. Adelman, Jr. Anderson, John E., Scott F. Anderson, James Annis, Neta A. Bahcall, J. A. Bakken, Robert Barkhouser, Steven Bastian, Eileen Berman, William N. Boroski, Steve Bracker, Charlie Briegel, John W. Briggs, J. Brinkmann, Robert Brunner, Scott Burles, Larry Carey, Michael A. Carr, Francisco J. Castander, Bing Chen, Patrick L. Colestock, A. J. Connolly, J. H. Crocker, István Csabai, Paul C. Czarapata, John Eric Davis, Mamoru Doi, Tom Dombeck, Daniel Eisenstein, Nancy Ellman, Brian R. Elms, Michael L. Evans, Xiaohui Fan, Glenn R. Federwitz, Larry Fiscelli, Scott Friedman, Joshua A. Frieman, Masataka Fukugita, Bruce Gillespie, James E. Gunn, Vijay K. Gurbani, Ernst de Haas, Merle Haldeman, Frederick H. Harris, J. Hayes, Timothy M. Heckman, G. S. Hennessy, Robert B. Hindsley, Scott Holm, Donald J. Holmgren, Chi-hao Huang, Charles Hull, Don Husby, Shin-Ichi Ichikawa, Takashi Ichikawa, Željko Ivezić, Stephen Kent, Rita S. J. Kim, E. Kinney, Mark Klaene, A. N. Kleinman, S. Kleinman, G. R. Knapp, John Korienek, Richard G. Kron, Peter Z. Kunszt, D. Q. Lamb, B. Lee, R. French Leger, Siriluk Limmongkol, Carl Lindenmeyer, Daniel C. Long, Craig Loomis, Jon Loveday, Rich Lucinio, Robert H. Lupton, Bryan MacKinnon, Edward J. Mannery, P. M. Mantsch, Bruce Margon, Peregrine McGehee, Timothy A. McKay, Avery Meiksin, Aronne Merelli, David G. Monet, Jeffrey A. Munn, Vijay K. Narayanan, Thomas Nash, Eric Neilsen, Rich Neswold, Heidi Jo Newberg, R. C. Nichol, Tom Nicinski, Mario Nonino, Norio Okada, Sadanori Okamura, Jeremiah P. Ostriker, Russell Owen, A. George Pauls, John Peoples, R. L. Peterson, Donald Petravick, Jeffrey R. Pier, Adrian Pope, Ruth Pordes, Angela Prosapio, Ron Rechenmacher, Thomas R. Quinn, Gordon T. Richards, Michael W. Richmond, Claudio H. Rivetta, Constance M. Rockosi, Kurt Ruthmansdorfer, Dale Sandford, David J. Schlegel, Donald P. Schneider, Maki Sekiguchi, Gary Sergey, Kazuhiro Shimasaku, Walter A. Siegmund, Stephen Smee, J. Allyn Smith, S. Snedden, R. Stone, Chris Stoughton, Michael A. Strauss, Christopher Stubbs, Mark SubbaRao, Alexander S. Szalay, Istvan Szapudi, Gyula P. Szokoly, Anirudda R. Thakar, Christy Tremonti, Douglas L. Tucker, Alan Uomoto, Dan Vanden Berk, Michael S. Vogeley, Patrick Waddell, Shu-i. Wang, Masaru Watanabe, David H. Weinberg, Brian Yanny, Naoki Yasuda, and SDSS Collaboration. The Sloan Digital Sky Survey: Technical Summary. AJ, 120(3):1579–1587, September 2000.

[35] Rachel Mandelbaum, Christopher M. Hirata, Mustapha Ishak, Uroš Seljak, and Jonathan Brinkmann. Detection of large-scale intrinsic ellipticity-density correlation from the Sloan Digital Sky Survey and implications for weak lensing surveys. MNRAS, 367(2):611–626, Apr 2006.

[36] Christopher M. Hirata, Rachel Mandelbaum, Mustapha Ishak, Uroš Seljak, Robert Nichol, Kevin A. Pimbblet, Nicholas P. Ross, and David Wake. Intrinsic galaxy alignments from the 2SLAQ and SDSS surveys: luminosity and redshift scalings and implications for weak lensing surveys. MNRAS, 381(3):1197–1218, November 2007.

[37] Teppei Okumura and Y. P. Jing. The Gravitational Shear-Intrinsic Ellipticity Correlation Functions of Luminous Red Galaxies in Observation and in the ΛCDM Model. ApJ, 694(1):L83–L86, March 2009.

[38] B. Joachimi, R. Mandelbaum, F. B. Abdalla, and S. L. Bridle. Constraints on intrinsic alignment contamination of weak lensing surveys using the MegaZ-LRG sample. A&A, 527:A26, Mar 2011.

[39] Cheng Li, Y. P. Jing, A. Faltenbacher, and Jie Wang. The Detection of the Large-scale Alignment of Massive Galaxies at z ~0.6. ApJ, 770(1):L12, June 2013.

[40] Y. P. Jing, H. J. Mo, and G. Börner. Spatial Correlation Function and Pairwise Velocity Dispersion of Galaxies: Cold Dark Matter Models versus the Las Campanas Survey. ApJ, 494(1):1–12, February 1998.

[41] Uroš Seljak. Analytic model for galaxy and dark matter clustering. MNRAS, 318(1):203–213, October 2000.

[42] J. A. Peacock and R. E. Smith. Halo occupation numbers and galaxy bias. MNRAS, 318(4):1144–1156, November 2000.

[43] Zheng Zheng, Andreas A. Berlind, David H. Weinberg, Andrew J. Benson, Carlton M. Baugh, Shaun Cole, Romeel Davé, Carlos S. Frenk, Neal Katz, and Cedric G. Lacey. Theoretical Models of the Halo Occupation Distribution: Separating Central and Satellite Galaxies. ApJ, 633(2):791–809, November 2005.

[44] Ananth Tenneti, Sukhdeep Singh, Rachel Mandelbaum, Tiziana di Matteo, Yu Feng, and Nishikanta Khandai. Intrinsic alignments of galaxies in the MassiveBlack-II simulation: analysis of two-point statistics. MNRAS, 448(4):3522–3544, April 2015.

[45] Ananth Tenneti, Rachel Mandelbaum, Tiziana Di Matteo, Alina Kiessling, and Nishikanta Khandai. Galaxy shapes and alignments in the massiveblack-ii hydrodynamic and dark matter-only simulations. *Monthly Notices of the Royal Astronomical Society*, 453(1):469–482, Aug 2015.

[46] Rachel Mandelbaum, Chris Blake, Sarah Bridle, Filipe B. Abdalla, Sarah Brough, Matthew Colless, Warrick Couch, Scott Croom, Tamara Davis, Michael J. Drinkwater, Karl Forster, Karl Glazebrook, Ben Jelliffe, Russell J. Jurek, I. Hui Li, Barry Madore, Chris Martin, Kevin Pimbblet, Gregory B. Poole, Michael Pracy, Rob Sharp, Emily Wisnioski, David Woods, and Ted Wyder. The WiggleZ Dark Energy Survey: direct constraints on blue galaxy intrinsic alignments at intermediate redshifts. MNRAS, 410(2):844–859, January 2011.

[47] Jingjing Shi, Toshiki Kurita, Masahiro Takada, Ken Osato, Yosuke Kobayashi, and Takahiro Nishimichi. Power Spectrum of Intrinsic Alignments of Galaxies in IllustrisTNG. *JCAP*, 03:030, 2021.

[48] G. M. Bernstein and M. Jarvis. Shapes and Shears, Stars and Smears: Optimal Measurements for Weak Lensing. AJ, 123(2):583–618, Feb 2002.

[49] James M. Bardeen. Gauge-invariant cosmological perturbations. Phys. Rev. D, 22(8):1882–1905, October 1980.

[50] Planck Collaboration, N. Aghanim, Y. Akrami, M. Ashdown, J. Aumont, C. Baccigalupi, M. Ballardini, A. J. Banday, R. B. Barreiro, N. Bartolo, S. Basak, R. Battye, K. Benabed, J. P. Bernard, M. Bersanelli, P. Bielewicz, J. J. Bock, J. R. Bond, J. Borrill, F. R. Bouchet, F. Boulanger, M. Bucher, C. Burigana, R. C. Butler, E. Calabrese, J. F. Cardoso, J. Carron, A. Challinor, H. C. Chiang, J. Chluba, L. P. L. Colombo, C. Combet, D. Contreras, B. P. Crill, F. Cuttaia, P. de Bernardis, G. de Zotti, J. Delabrouille, J. M. Delouis, E. Di Valentino, J. M. Diego, O. Doré, M. Douspis, A. Ducout, X. Dupac, S. Dusini, G. Efstathiou, F. Elsner, T. A. Enßlin, H. K. Eriksen, Y. Fantaye, M. Farhang, J. Fergusson, R. Fernandez-Cobos, F. Finelli, F. Forastieri, M. Frailis, A. A. Fraisse, E. Franceschi, A. Frolov, S. Galeotta, S. Galli, K. Ganga, R. T. Génova-Santos, M. Gerbino, T. Ghosh, J. González-Nuevo, K. M. Górski, S. Gratton, A. Gruppuso, J. E. Gudmundsson, J. Hamann, W. Handley, F. K. Hansen, D. Herranz, S. R. Hildebrandt, E. Hivon, Z. Huang, A. H. Jaffe, W. C. Jones, A. Karakci, E. Keihänen, R. Keskitalo, K. Kiiveri, J. Kim, T. S. Kisner, L. Knox, N. Krachmalnicoff, M. Kunz, H. Kurki-Suonio, G. Lagache, J. M. Lamarre, A. Lasenby, M. Lattanzi, C. R. Lawrence, M. Le Jeune, P. Lemos, J. Lesgourgues, F. Levrier, A. Lewis, M. Liguori, P. B. Lilje, M. Lilley, V. Lindholm, M. López-Caniego, P. M. Lubin, Y. Z. Ma, J. F. Macías-Pérez, G. Maggio, D. Maino, N. Mandolesi, A. Mangilli, A. Marcos-Caballero, M. Maris, P. G. Martin, M. Martinelli, E. Martínez-González, S. Matarrese, N. Mauri, J. D. McEwen, P. R. Meinhold, A. Melchiorri, A. Mennella, M. Migliaccio, M. Millea, S. Mitra, M. A. Miville-Deschênes, D. Molinari, L. Montier, G. Morgante, A. Moss, P. Natoli, H. U. Nørgaard-Nielsen, L. Pagano, D. Paoletti, B. Partridge, G. Patanchon, H. V. Peiris, F. Perrotta, V. Pettorino, F. Piacentini, L. Polastri, G. Polenta, J. L. Puget, J. P. Rachen, M. Reinecke, M. Remazeilles, A. Renzi, G. Rocha, C. Rosset, G. Roudier, J. A. Rubiño-Martín,

B. Ruiz-Granados, L. Salvati, M. Sandri, M. Savelainen, D. Scott, E. P. S. Shellard, C. Sirignano, G. Sirri, L. D. Spencer, R. Sunyaev, A. S. Suur-Uski, J. A. Tauber, D. Tavagnacco, M. Tenti, L. Toffolatti, M. Tomasi, T. Trombetti, L. Valenziano, J. Valiviita, B. Van Tent, L. Vibert, P. Vielva, F. Villa, N. Vittorio, B. D. Wandelt, I. K. Wehus, M. White, S. D. M. White, A. Zacchei, and A. Zonca. Planck 2018 results. VI. Cosmological parameters. A&A, 641:A6, September 2020.

[51] Eiichiro Komatsu and David N. Spergel. Acoustic signatures in the primary microwave background bispectrum. Phys. Rev. D, 63(6):063002, March 2001.

[52] E. Komatsu, A. Kogut, M. R. Nolta, C. L. Bennett, M. Halpern, G. Hinshaw, N. Jarosik, M. Limon, S. S. Meyer, L. Page, D. N. Spergel, G. S. Tucker, L. Verde, E. Wollack, and E. L. Wright. First-Year Wilkinson Microwave Anisotropy Probe (WMAP) Observations: Tests of Gaussianity. ApJS, 148(1):119–134, September 2003.

[53] D. N. Spergel, R. Bean, O. Doré, M. R. Nolta, C. L. Bennett, J. Dunkley, G. Hinshaw, N. Jarosik, E. Komatsu, L. Page, H. V. Peiris, L. Verde, M. Halpern, R. S. Hill, A. Kogut, M. Limon, S. S. Meyer, N. Odegard, G. S. Tucker, J. L. Weiland, E. Wollack, and E. L. Wright. Three-Year Wilkinson Microwave Anisotropy Probe (WMAP) Observations: Implications for Cosmology. ApJS, 170(2):377–408, June 2007.

[54] E. Komatsu, K. M. Smith, J. Dunkley, C. L. Bennett, B. Gold, G. Hinshaw, N. Jarosik, D. Larson, M. R. Nolta, L. Page, D. N. Spergel, M. Halpern, R. S. Hill, A. Kogut, M. Limon, S. S. Meyer, N. Odegard, G. S. Tucker, J. L. Weiland, E. Wollack, and E. L. Wright. Seven-year Wilkinson Microwave Anisotropy Probe (WMAP) Observations: Cosmological Interpretation. ApJS, 192(2):18, February 2011.

[55] Planck Collaboration, P. A. R. Ade, N. Aghanim, M. Arnaud, F. Arroja, M. Ashdown, J. Aumont, C. Baccigalupi, M. Ballardini, A. J. Banday, R. B. Barreiro, N. Bartolo, S. Basak, E. Battaner, K. Benabed, A. Benoît, A. Benoit-Lévy, J. P. Bernard, M. Bersanelli, P. Bielewicz, J. J. Bock, A. Bonaldi, L. Bonavera, J. R. Bond, J. Borrill, F. R. Bouchet, F. Boulanger, M. Bucher, C. Burigana, R. C. Butler, E. Calabrese, J. F. Cardoso, A. Catalano, A. Challinor, A. Chamballu, H. C. Chiang, P. R. Christensen, S. Church, D. L. Clements, S. Colombi, L. P. L. Colombo, C. Combet, F. Couchot, A. Coulais, B. P. Crill, A. Curto, F. Cuttaia, L. Danese, R. D. Davies, R. J. Davis, P. de Bernardis, A. de Rosa, G. de Zotti, J. Delabrouille, F. X. Désert, J. M. Diego, H. Dole, S. Donzelli, O. Doré, M. Douspis, A. Ducout, X. Dupac, G. Efstathiou, F. Elsner, T. A. Enßlin, H. K. Eriksen, J. Fergusson, F. Finelli, O. Forni, M. Frailis, A. A. Fraisse, E. Franceschi, A. Frejsel, S. Galeotta, S. Galli, K. Ganga, C. Gauthier, T. Ghosh, M. Giard, Y. Giraud-Héraud, E. Gjerløw, J. González-Nuevo, K. M. Górski, S. Gratton, A. Gregorio, A. Gruppuso, J. E. Gudmundsson,

J. Hamann, F. K. Hansen, D. Hanson, D. L. Harrison, A. Heavens, G. Helou, S. Henrot-Versillé, C. Hernández-Monteagudo, D. Herranz, S. R. Hildebrandt, E. Hivon, M. Hobson, W. A. Holmes, A. Hornstrup, W. Hovest, Z. Huang, K. M. Huffenberger, G. Hurier, A. H. Jaffe, T. R. Jaffe, W. C. Jones, M. Juvela, E. Keihänen, R. Keskitalo, J. Kim, T. S. Kisner, J. Knoche, M. Kunz, H. Kurki-Suonio, F. Lacasa, G. Lagache, A. Lähteenmäki, J. M. Lamarre, A. Lasenby, M. Lattanzi, C. R. Lawrence, R. Leonardi, J. Lesgourgues, F. Levrier, A. Lewis, M. Liguori, P. B. Lilje, M. Linden-Vørnle, M. López-Caniego, P. M. Lubin, J. F. Macías-Pérez, G. Maggio, D. Maino, N. Mandolesi, A. Mangilli, D. Marinucci, M. Maris, P. G. Martin, E. Martínez-González, S. Masi, S. Matarrese, P. McGehee, P. R. Meinhold, A. Melchiorri, L. Mendes, A. Mennella, M. Migliaccio, S. Mitra, M. A. Miville-Deschênes, A. Moneti, L. Montier, G. Morgante, D. Mortlock, A. Moss, M. Münchmeyer, D. Munshi, J. A. Murphy, P. Naselsky, F. Nati, P. Natoli, C. B. Netterfield, H. U. Nørgaard-Nielsen, F. Noviello, D. Novikov, I. Novikov, C. A. Oxborrow, F. Paci, L. Pagano, F. Pajot, D. Paoletti, F. Pasian, G. Patanchon, H. V. Peiris, O. Perdereau, L. Perotto, F. Perrotta, V. Pettorino, F. Piacentini, M. Piat, E. Pierpaoli, D. Pietrobon, S. Plaszczynski, E. Pointecouteau, G. Polenta, L. Popa, G. W. Pratt, G. Prézeau, S. Prunet, J. L. Puget, J. P. Rachen, B. Racine, R. Rebolo, M. Reinecke, M. Remazeilles, C. Renault, A. Renzi, I. Ristorcelli, G. Rocha, C. Rosset, M. Rossetti, G. Roudier, J. A. Rubiño-Martín, B. Rusholme, M. Sandri, D. Santos, M. Savelainen, G. Savini, D. Scott, M. D. Seiffert, E. P. S. Shellard, M. Shiraishi, K. Smith, L. D. Spencer, V. Stolyarov, R. Stompor, R. Sudiwala, R. Sunyaev, P. Sutter, D. Sutton, A. S. Suur-Uski, J. F. Sygnet, J. A. Tauber, L. Terenzi, L. Toffolatti, M. Tomasi, M. Tristram, A. Troja, M. Tucci, J. Tuovinen, L. Valenziano, J. Valiviita, B. Van Tent, P. Vielva, F. Villa, L. A. Wade, B. D. Wandelt, I. K. Wehus, D. Yvon, A. Zacchei, and A. Zonca. Planck 2015 results. XVII. Constraints on primordial non-Gaussianity. A&A, 594:A17, September 2016.

[56] Planck Collaboration, Y. Akrami, F. Arroja, M. Ashdown, J. Aumont, C. Baccigalupi, M. Ballardini, A. J. Banday, R. B. Barreiro, N. Bartolo, S. Basak, K. Benabed, J. P. Bernard, M. Bersanelli, P. Bielewicz, J. R. Bond, J. Borrill, F. R. Bouchet, M. Bucher, C. Burigana, R. C. Butler, E. Calabrese, J. F. Cardoso, B. Casaponsa, A. Challinor, H. C. Chiang, L. P. L. Colombo, C. Combet, B. P. Crill, F. Cuttaia, P. de Bernardis, A. de Rosa, G. de Zotti, J. Delabrouille, J. M. Delouis, E. Di Valentino, J. M. Diego, O. Doré, M. Douspis, A. Ducout, X. Dupac, S. Dusini, G. Efstathiou, F. Elsner, T. A. Enßlin, H. K. Eriksen, Y. Fantaye, J. Fergusson, R. Fernandez-Cobos, F. Finelli, M. Frailis, A. A. Fraisse, E. Franceschi, A. Frolov, S. Galeotta, S. Galli, K. Ganga, R. T. Génova-Santos, M. Gerbino, J. González-Nuevo, K. M. Górski, S. Gratton, A. Gruppuso, J. E. Gudmundsson, J. Hamann, W. Handley, F. K. Hansen, D. Herranz, E. Hivon, Z. Huang, A. H. Jaffe, W. C. Jones, G. Jung, E. Keihänen, R. Keskitalo, K. Kiiveri, J. Kim, N. Krachmalnicoff, M. Kunz, H. Kurki-Suonio, J. M. Lamarre, A. Lasenby, M. Lattanzi, C. R. Lawrence, M. Le

Jeune, F. Levrier, A. Lewis, M. Liguori, P. B. Lilje, V. Lindholm, M. López-Caniego, Y. Z. Ma, J. F. Macías-Pérez, G. Maggio, D. Maino, N. Mandolesi, A. Marcos-Caballero, M. Maris, P. G. Martin, E. Martínez-González, S. Matarrese, N. Mauri, J. D. McEwen, P. D. Meerburg, P. R. Meinhold, A. Melchiorri, A. Mennella, M. Migliaccio, M. A. Miville-Deschênes, D. Molinari, A. Moneti, L. Montier, G. Morgante, A. Moss, M. Münchmeyer, P. Natoli, F. Oppizzi, L. Pagano, D. Paoletti, B. Partridge, G. Patanchon, F. Perrotta, V. Pettorino, F. Piacentini, G. Polenta, J. L. Puget, J. P. Rachen, B. Racine, M. Reinecke, M. Remazeilles, A. Renzi, G. Rocha, J. A. Rubiño-Martín, B. Ruiz-Granados, L. Salvati, M. Savelainen, D. Scott, E. P. S. Shellard, M. Shiraishi, C. Sirignano, G. Sirri, K. Smith, L. D. Spencer, L. Stanco, R. Sunyaev, A. S. Suur-Uski, J. A. Tauber, D. Tavagnacco, M. Tenti, L. Toffolatti, M. Tomasi, T. Trombetti, J. Valiviita, B. Van Tent, P. Vielva, F. Villa, N. Vittorio, B. D. Wandelt, I. K. Wehus, A. Zacchei, and A. Zonca. Planck 2018 results. IX. Constraints on primordial non-Gaussianity. A&A, 641:A9, September 2020.

[57] Maresuke Shiraishi, Eiichiro Komatsu, Marco Peloso, and Neil Barnaby. Signatures of anisotropic sources in the squeezed-limit bispectrum of the cosmic microwave background. J. Cosmology Astropart. Phys., 2013(5):002, May 2013.

[58] Solomon Endlich, Alberto Nicolis, and Junpu Wang. Solid inflation. J. Cosmology Astropart. Phys., 2013(10):011, October 2013.

[59] Ivan Agullo and Sarah Shandera. Large non-Gaussian halo bias from single field inflation. J. Cosmology Astropart. Phys., 2012(9):007, September 2012.

[60] Nicola Bartolo, Sabino Matarrese, Marco Peloso, and Angelo Ricciardone. Anisotropic power spectrum and bispectrum in the $f(\phi)F^2$ mechanism. Phys. Rev. D, 87(2):023504, January 2013.

[61] Maresuke Shiraishi. Parity violation of primordial magnetic fields in the CMB bispectrum. J. Cosmology Astropart. Phys., 2012(6):015, June 2012.

[62] Maresuke Shiraishi, Daisuke Nitta, Shuichiro Yokoyama, and Kiyotomo Ichiki. Optimal limits on primordial magnetic fields from CMB temperature bispectrum of passive modes. J. Cosmology Astropart. Phys., 2012(3):041, March 2012.

[63] Nicola Bartolo, Sabino Matarrese, Marco Peloso, and Maresuke Shiraishi. Parity-violating CMB correlators with non-decaying statistical anisotropy. J. Cosmology Astropart. Phys., 2015(7):039–039, July 2015.

[64] Nima Arkani-Hamed and Juan Maldacena. Cosmological Collider Physics. *arXiv e-prints*, page arXiv:1503.08043, March 2015.

[65] Hayden Lee, Daniel Baumann, and Guilherme L. Pimentel. Non-Gaussianity as a particle detector. *Journal of High Energy Physics*, 2016(12):40, December 2016.

[66] Gabriele Franciolini, Alex Kehagias, Antonio Riotto, and Maresuke Shiraishi. Detecting higher spin fields through statistical anisotropy in the CMB bispectrum. Phys. Rev. D, 98(4):043533, August 2018.

[67] Kazuyuki Akitsu, Toshiki Kurita, Takahiro Nishimichi, Masahiro Takada, and Satoshi Tanaka. Imprint of anisotropic primordial non-Gaussianity on halo intrinsic alignments in simulations. Phys. Rev. D, 103(8):083508, April 2021.

[68] Neal Dalal, Olivier Doré, Dragan Huterer, and Alexander Shirokov. Imprints of primordial non-Gaussianities on large-scale structure: Scale-dependent bias and abundance of virialized objects. Phys. Rev. D, 77(12):123514, June 2008.

[69] Toshiki Kurita and Masahiro Takada. Constraints on anisotropic primordial non-Gaussianity from intrinsic alignments of SDSS-III BOSS galaxies. Phys. Rev. D, 108(8):083533, October 2023.